Petroleum Science 21 (2024) 1796–1813

Contents lists available at ScienceDirect

Petroleum Science

journal homepage: www.keaipublishing.com/en/journals/petroleum-science

Original Paper

Production induced fracture closure of deep shale gas well under thermo-hydro-mechanical conditions

Shi-Ming Wei [a], Yang Xia [a], Yan Jin [a, *], Xu-Yang Guo [a], Jing-Yu Zi [b], Kai-Xuan Qiu [c, **], Si-Yuan Chen [a]

[a] College of Science, China University of Petroleum (Beijing), Beijing, 102249, China
[b] CNOOC Research Institute Ltd, Beijing, 100028, China
[c] The University of Hong Kong, Hong Kong, 999077, China

ARTICLE INFO

Article history:
Received 2 May 2023
Received in revised form
11 December 2023
Accepted 12 December 2023
Available online 20 December 2023

Edited by Yan-Hua Sun

Keywords:
Shale gas
Fracture closure
Fluid–solid–heat coupling
Discontinuous discrete fracture

ABSTRACT

Deep shale gas reservoirs have geological characteristics of high temperature, high pressure, high stress, and inferior ability to pass through fluids. The multi-stage fractured horizontal well is the key to exploiting the deep shale gas reservoir. However, during the production process, the effectiveness of the hydraulic fracture network decreases with the closure of fractures, which accelerates the decline of shale gas production. In this paper, we addressed the problems of unclear fracture closure mechanisms and low accuracy of shale gas production prediction during deep shale gas production. Then we established the fluid–solid–heat coupled model coupling the deformation and fluid flow among the fracture surface, proppant and the shale matrix. When the fluid–solid–heat coupled model was applied to the fracture network, it was well solved by our numerical method named discontinuous discrete fracture method. Compared with the conventional discrete fracture method, the discontinuous discrete fracture method can describe the three-dimensional morphology of the fracture while considering the effect of the change of fracture surface permeation coefficient on the coupled fracture–matrix flow and describing the displacement discontinuity across the fracture. Numerical simulations revealed that the degree of fracture closure increases as the production time proceeds, and the degree of closure of the secondary fractures is higher than that of the primary fractures. Shale creep and proppant embedment both increase the degree of fracture closure. The reduction in fracture surface permeability due to proppant embedment reduces the rate of fluid transfer between matrix and fracture, which has often been overlooked in the past. However, it significantly impacts shale gas production, with calculations showing a 24.7% cumulative three-year yield reduction. This study is helpful to understand the mechanism of hydraulic fracture closure. Therefore, it provides the theoretical guidance for maintaining the long-term effectiveness of hydraulic fractures.

1. Introduction

Most of the shale gas enrichment layers in the Sichuan Basin of China are deep shale gas with a burial depth of more than 3500 m. A large-scale long-effective hydraulic fracture network is the key technology to realize the economic exploitation of deep shale gas. Therefore, in deep shale gas production, the study of fracture closure mechanism under high temperature, high pressure and high closure stress has a critical guiding significance for increasing and stabilizing deep shale gas production. The research purpose of fracture closure is to maintain the maximum hydraulic fracture conductivity as much as possible, that is, the effective fracture width. However, is fracture conductivity the only factor affecting the shale gas production of hydraulic fractures? Is the fracture conductivity the higher, the better?

The change in formation pressure causes the multi-field coupling problem in the production process. The correct shale gas flow mechanism is the basis for accurately calculating formation pressure. Freeman et al. (2013) found that the seepage model based

* Corresponding author.
** Corresponding author.
E-mail addresses: jiny@cup.edu.cn (Y. Jin), qiukx940908@163.com (K.-X. Qiu).

https://doi.org/10.1016/j.petsci.2023.12.010

on Darcy's law cannot explain the production data of shale gas reservoirs, and they proposed that the diffusion effect is the leading way to tight gas flow. Cronin et al. (2019) considered diffusion the primary control mechanism of fluid flow in tight reservoirs and gave the mass concentration diffusion equation based on Fick's law without considering the influence of Darcy flow. The established diffusion model can well explain the field production data. Based on the N–S equation of compressible fluid and the theory of small Mach number flow (Klainerman and Majda, 1982), Jin and Chen (2019) established the control equation of gas self-diffusion flow in the primary exploitation of tight gas, pointing out that diffusion is the primary flow mechanism of low porosity and low permeability reservoirs. Jin et al. (2020) fitted the production of shale gas wells in Sichuan, China, based on the self-diffusion flow equation at the macro scale and found that the yield fitting results were significantly better than the conventional Darcy and Knudsen diffusion models. In this paper, the self-diffusion equation is used to describe the flow of shale gas.

The fluid–solid coupling model is the theoretical basis for simulating the fracture closure process. Valliappan and Khalili-Naghadeh (1990) derived the effective stress coefficients of two pressure systems based on the dual-porosity medium model by considering the porosity changes of matrix pores and natural fractures, respectively. Based on the fluid–solid coupling model of double porous media, Lu et al. (2021) deduced the fluid–solid coupling model of triple porous media. The multi-medium model treats natural fractures as continuous media and cannot describe the local flow characteristics of natural fractures. Researchers have proposed a discrete fracture model to solve the flow in natural fractures and matrices, respectively. However, the discrete fracture model applies the effective stress principle to couple the pressure and stress fields. Due to the continuity of the pressure field, the stress field and displacement field are also continuous, which makes the discrete fracture model unable to capture the mechanical interaction mechanism between hydraulic fractures and natural fractures. Wei et al. (2021) modified the discrete fracture model and proposed a discontinuous discrete fracture model, which realized the description of discontinuous displacement and the spatial configuration of fractures.

After hydraulic fracturing in oil and gas reservoirs, the fracture closure has a significant impact on the fluid flow process, especially on the long-term production process. Zhou et al. (2019) proposed a fluid–solid coupling model in the early flowback process of shale oil reservoirs and solved it by the finite element method. Zhou's results showed that the fracture closure was uneven during the flowback process. Excessive production pressure drop may destroy the connectivity between fractures and the wellbore. Liu et al. (2019) considered the effects of fracture closure and uneven proppant distribution when simulating fracturing fluid distribution and shale gas recovery. The numerical simulation showed that if the fracture width in the closure process was neglected, the final recovery factor would be about 40% higher. Lacy et al. (1998) believed that the proppant embedment would reduce the fracture width by 10%–60% and reduce the oil and gas production. Reducing fracture width by 20% may reduce the recovery rate by 50%–60%. According to Fan et al. (2010), the excessive pressure drop will lead to fracture closure, resulting in some fractures disconnected from the wellbore, thereby reducing oil and gas well recovery. Yan et al. (2020) simulated the fluid–solid coupling process of fractured shale reservoirs using an efficient hybrid model composed of multiple continua and embedded discrete fracture models (EDFM). They studied the effect of partial support fracture closure on reservoir gas production. The current numerical simulation work evaluates the influence of fracture width, or fracture conductivity change, on the production of fractured wells. The reason is that the current numerical model only considers the influence of fracture conductivity on fracture-matrix coupling flow and fails to consider the influence of fracture surface properties on fracture–matrix coupling flow.

In this paper, the fracture closure process is regarded as the fracture–proppant–matrix coupling deformation process, and a fluid–solid–heat coupled model for the fracture closure process is established. The discontinuous discrete fracture model is used to describe the fracture network. The influence of the permeation coefficient of the fracture surface on the fracture–matrix coupling flow and the actual morphology of the fracture is considered. The finite element method is used to solve the coupling model.

2. Mathematical model

2.1. Governing equations

Considering temperature, fluid pressure and adsorbed gas desorption, the total stress of shale can be expressed as follows:

$$\boldsymbol{\sigma}=\boldsymbol{\sigma}_0+\boldsymbol{D}:[\boldsymbol{\varepsilon}+\alpha_s(T_s-T_{s0})\boldsymbol{I}]+\alpha_b(p_0-p)\boldsymbol{I}-K\varepsilon_L\frac{p}{p+p_L}\boldsymbol{I} \tag{1}$$

where $\boldsymbol{\sigma}_0$ is the *in-situ* geo-stress field, MPa; $\boldsymbol{\varepsilon}$ is the skeleton strain; α_s is the coefficient of thermal expansion of the shale matrix, 1/K; T_s is the temperature of the shale matrix, K; T_{s0} is the original formation temperature, K; α_b is the effective stress coefficient; p and p_0 are respectively the current pore pressure and the initial pore pressure, MPa; K is the bulk modulus of rock skeleton, MPa; ε_L is the Langmuir strain constant indicating the influence of adsorbed gas desorption on rock deformation; p_L is the Langmuir pressure, MPa; $\boldsymbol{I}$ is the identity diagonal matrix; $\boldsymbol{D}$ is the stiffness matrix of dry rock, and for the homogeneous rock, it can be expressed as

$$\boldsymbol{D}=\frac{E}{(1+\nu)(1-2\nu)}\begin{bmatrix}1-\nu & \nu & \nu & 0 & 0 & 0\\ \nu & 1-\nu & \nu & 0 & 0 & 0\\ \nu & \nu & 1-\nu & 0 & 0 & 0\\ 0 & 0 & 0 & 1-2\nu & 0 & 0\\ 0 & 0 & 0 & 0 & 1-2\nu & 0\\ 0 & 0 & 0 & 0 & 0 & 1-2\nu\end{bmatrix} \tag{2}$$

where E is the elastic modulus, MPa; ν is Poisson's ratio.

Considering the quasi-static process of solid deformation, the stress balance equation is

$$\nabla\cdot\boldsymbol{\sigma}+\rho_s\boldsymbol{g}=0 \tag{3}$$

where $\boldsymbol{g}$ is the gravitational acceleration, m/s^2; ρ_s is the rock density, kg/m^3.

The formation pressure decreases continuously during the production process, and the area of formation pressure reduction increases continuously with the increase in production time, so the adsorbed gas desorption process will always be in a dynamic nonequilibrium process. Gas adsorption can be described using the nonequilibrium Langmuir equation:

$$R_{ad}=k_a(1-\theta)\rho_{ga} \tag{4}$$

The desorption process of adsorbed gas can be described by Henry's theorem:

$$R_{de}=k_d\rho_{gs} \tag{5}$$

where R_{ad} is the mass of adsorbed gas per unit volume of rock per unit time, kg/(m^3 s); k_a is the adsorption rate of free gas, 1/s; ρ_{ga} is

the density of free gas, kg/m^3; R_{de} is the mass of desorbed gas per unit volume of rock per unit time, kg/(m^3 s); k_d is the desorption rate of the adsorbed gas, 1/s; ρ_{gs} is the density of the adsorbed gas, kg/m^3; θ is the ratio of the occupied adsorption sites to all adsorption sites in inner pore surfaces, and $\theta = \rho_{gs}/\rho_{gsm}$; ρ_{gsm} is the density when the concentration of adsorbed gas reaches the maximum, that is, the maximum adsorption capacity of shale, kg/m^3.

The net desorption rate per unit volume of shale can be written as

$$R_{net} = R_{de} - R_{net} = k_d\rho_{gs} - k_a(1-\theta)\rho_{ga} \tag{6}$$

Some previous literature reported that shale gas transportation was controlled by diffusion mechanisms (Freeman et al., 2013; Cronin et al., 2019; Jin and Chen, 2019). In this paper, the self-diffusion model is employed to formulate the free shale gas flow (Jin and Chen, 2019). Combining the dynamic desorption of the adsorbed gas, the transportation of the shale gas can be described using the equation below.

$$\frac{\partial(\phi\rho_{ga})}{\partial t} - \nabla\cdot\left(D_{eff}\nabla\rho_{ga}\right) = R_{net} \tag{7}$$

$$D_{eff} = \frac{\mu_b + 4\mu/3}{\rho} \tag{8}$$

where D_{eff} is the effective self-diffusivity of gas, m^2/s.

Surface diffusion of adsorbed gas also occurs on the solid surface (Wei et al., 2019). The governing equation of adsorbed gas is

$$\frac{\partial\rho_{gs}}{\partial t} - D_S\nabla\cdot(\nabla\rho_{gs}) = -R_{net} \tag{9}$$

where D_S is the surface diffusion coefficient of adsorbed gas, m^2/s.

Deep shale gas reservoirs are characterized with high temperature and high pressure. Fracturing fluid injection and flowback in the fracturing process can bring great heat loss to the formation, especially in the area near hydraulic fractures. At this point, the influence of temperature on gas properties must be considered. The density and pressure of real gas can be formulated by the state equation:

$$pV_L = ZRT, \quad \rho_g = pM/(ZRT) \tag{10}$$

where V_L is the molar volume of gas under the temperature T, m^3/mol; ρ_g is the density of gas, kg/m^3; R is the thermodynamic constant, 8.314 J/(mol K); M is the molecular mass, kg/mol; Z is the gas compression factor. Since the critical temperature of methane is −82.56 °C, the adsorbed gas under the formation condition is also gaseous, so Eq. (10) is used for both free gas and adsorbed gas.

The gas compression factor and shear viscosity of gas vary with gas composition, pressure and temperature. The empirical formula of Heidaryan et al. (2010) is adopted in this paper. The compression factor and shear viscosity of methane can be expressed as follows:

$$Z = \ln\left[\frac{A_1 + A_3\ln p_{pr} + \frac{A_5}{T_{pr}} + A_7\left(\ln p_{pr}\right)^2 + \frac{A_9}{T_{pr}^2} + \frac{A_{11}}{T_{pr}}\ln p_{pr}}{1 + A_2\ln p_{pr} + \frac{A_4}{T_{pr}} + A_6\left(\ln p_{pr}\right)^2 + \frac{A_8}{T_{pr}^2} + \frac{A_{10}}{T_{pr}}\ln p_{pr}}\right] \tag{11}$$

$$\mu = \ln\left[\frac{B_1 + (B_2+B_3)\left(\frac{M}{T}\right) + B_4\rho_{ga} + B_5\rho_{ga}^2 + B_6\rho_{ga}^3}{1 + B_7\left(\frac{M}{T}\right) + B_8\left(\frac{M}{T}\right)^2 + B_9\left(\frac{M}{T}\right)^3 + B_{10}\rho_{ga}}\right] \tag{12}$$

$$p_{pr} = p/p_{pc} \tag{13}$$

$$T_{pr} = T/T_{pc} \tag{14}$$

where p_{pr} is the gas contrast pressure, MPa; T_{pr} is the gas contrast temperature, K; p_{pc} is the critical gas pressure, MPa; T_{pc} is the critical gas temperature, K; T is the gas temperature, K; A_i and B_i are the calculated coefficients obtained from the experiment, as shown in Table 1.

The thermal convection caused by the temperature field can be expressed by Eq. (15):

$$q_{g"TT5843c571""ADT} = -\rho_{ga}\beta_T\nabla T \tag{15}$$

where β_T is the heat conductivity, m^2/(s K).

Therefore, the gas mass flow rate after considering heat convection can be written as

$$q_g = -D_{eff}\nabla\rho_{ga} - \rho_{ga}\beta_T\nabla T \tag{16}$$

Using Eq. (16) to modify the self-diffusion flow model, we can obtain the governing equation of shale gas flow considering the influence of the temperature field:

$$\frac{\partial(\phi\rho_{ga})}{\partial t} - \nabla\cdot\left(D_{eff}\nabla\rho_{ga} + \rho_{ga}\beta_T\nabla T\right) = R_{net} \tag{17}$$

If the rock is considered a slightly compressible porous medium, then we have the following:

$$\begin{aligned}\frac{\partial(\phi\rho_{ga})}{\partial t} &= \rho_{ga}\phi c_s\frac{\partial p}{\partial t} + \frac{\phi M}{RT}\frac{\partial}{\partial t}\left(\frac{p}{Z}\right)\\ &= c_s\frac{\phi Mp}{ZRT}\frac{\partial p}{\partial t} + \frac{\phi Mp}{ZRT}\left(\frac{1}{p} - \frac{1}{Z}\frac{\partial Z}{\partial p}\right)\frac{\partial p}{\partial t}\\ &= \left[\frac{\phi Mp}{ZRT}\left(c_s + \frac{1}{p} - \frac{1}{Z}\frac{\partial Z}{\partial p}\right)\right]\frac{\partial p}{\partial t} = \rho_{ga}\phi\left(c_s + \frac{1}{p} - \frac{1}{Z}\frac{\partial Z}{\partial p}\right)\frac{\partial p}{\partial t}\end{aligned} \tag{18}$$

Considering the real gas effect caused by pressure and temperature changes, the gas mass flow rate can be written as

Table 1
Real gas calculation coefficients (Heidaryan et al., 2010).

Coefficient for Z	Value		Coefficient for μ	Value
	$0.2 < p_{pr} < 3$	$p_{pr} > 3$		
A_1	2.827793	3.252838	B_1	1.022872
A_2	−0.468820	−0.13064	B_2	−1.651432
A_3	−1.262290	−0.64492	B_3	5.757386
A_4	−1.536520	−1.51803	B_4	-7.389×10^{-2}
A_5	−4.535050	−5.39102	B_5	8.389×10^{-2}
A_6	0.068951	−0.01380	B_6	2.977×10^{-1}
A_7	0.190387	0.066006	B_7	−1.451318
A_8	0.620000	0.612078	B_8	4.682506
A_9	1.838479	2.317431	B_9	1.918239
A_{10}	0.405237	0.163222	B_{10}	-9.945×10^{-2}
A_{11}	1.073574	0.56606		

$$-D_{\text{eff}}\nabla\rho_{\text{a}} = -D_{\text{eff}}\left(\frac{M}{ZRT}\nabla p + \frac{pM}{ZR}\nabla\frac{1}{T} + \frac{pM}{RT}\nabla\frac{1}{Z}\right)$$
$$= -D_{\text{eff}}\left[\frac{M}{ZRT}\nabla p - \frac{pM}{ZRT^2}\nabla T - \frac{pM}{RTZ^2}\left(\frac{\partial Z}{\partial p}\nabla p + \frac{\partial Z}{\partial T}\nabla T\right)\right] \tag{19}$$
$$= -D_{\text{eff}}\left[\rho_{\text{ga}}\left(\frac{1}{p} - \frac{1}{Z}\frac{\partial Z}{\partial p}\right)\nabla p - \rho_{\text{ga}}\left(\frac{1}{T} + \frac{1}{Z}\frac{\partial Z}{\partial T}\right)\nabla T\right]$$

Substituting Eqs. (18) and (19) into Eq. (17), Eq. (17) can be written as follows:

$$\rho_{\text{ga}}\phi(c_{\text{s}} + Z_{\text{p}})\frac{\partial p}{\partial t} - \nabla\cdot\left[\rho_{\text{ga}}Z_{\text{p}}D_{\text{eff}}\nabla p + \rho_{\text{ga}}(\beta_{\text{T}} + Z_{\text{T}})\nabla T\right] = R_{\text{net}} \tag{20}$$

$$Z_{\text{p}} = \frac{1}{p} - \frac{1}{Z}\frac{\partial Z}{\partial p} \tag{21}$$

$$Z_{\text{T}} = \frac{1}{T} + \frac{1}{Z}\frac{\partial Z}{\partial T} \tag{22}$$

When gas flow caused by rock deformation is taken into account, the governing equation of shale gas flow can be written as

$$\rho_{\text{ga}}\phi(c_{\text{s}} + Z_{\text{p}})\frac{\partial p}{\partial t} + \rho_{\text{ga}}(\alpha - \phi)\frac{\partial \varepsilon_{\text{v}}}{\partial t} - \nabla\cdot\left[\rho_{\text{ga}}Z_{\text{p}}D_{\text{eff}}\nabla p + \rho_{\text{ga}}(\beta_{\text{T}} + Z_{\text{T}})\nabla T_{\text{g}}\right] = R_{\text{net}} \tag{23}$$

Due to the limited heat transfer efficiency between gas and solid, the temperature in gas and solid is not the same, and this phenomenon is called local thermal nonequilibrium (Gao et al., 2017). Considering heat exchange brought by gas flow, the governing equation of the gas temperature field can be expressed by Eq. (24) (Xia et al., 2021; Detournay et al., 2022):

$$\phi\rho_{\text{ga}}C_{\text{g}}\frac{\partial T_{\text{g}}}{\partial t} - \eta_{\text{g1}}\nabla^2 T_{\text{g}} - \eta_{\text{g2}}\nabla^2 p = Q_{\text{Tf}} \tag{24}$$

$$\eta_{\text{g1}} = \phi k_{\text{g}} + \beta_{\text{T}}T(Z_{\text{T}}/Z_{\text{p}} - \rho_{\text{ga}}C_{\text{g}}) \tag{25}$$

$$\eta_{\text{g2}} = -T_{\text{g}}\left[\beta_{\text{T}} + (Z_{\text{T}}/Z_{\text{p}} - \rho_{\text{ga}}C_{\text{g}})\frac{D_{\text{eff}}}{p}\right] \tag{26}$$

$$Q_{\text{Tf}} = \frac{q_{\text{sf}}}{1-\phi}(T_{\text{s}} - T_{\text{g}}) \tag{27}$$

where C_{g} is the specific heat of gas, J/(kg K); q_{sf} is the interstitial convective heat transfer coefficient, J/(m^3 K s); T_{g} is the gas temperature, K; T_{s} is the rock temperature, K.

The governing equation of the rock temperature field is:

$$\rho_{\text{s}}C_{\text{s}}\frac{\partial T_{\text{s}}}{\partial t} + \nabla(-k_{\text{s}}\nabla T_{\text{s}}) = Q_{\text{Ts}} \tag{28}$$

$$Q_{\text{Ts}} = \frac{q_{\text{sf}}}{\phi}(T_{\text{g}} - T_{\text{s}}) \tag{29}$$

where C_{s} is the specific heat capacity of the rock, J/(kg K); K_{s} is the thermal conductivity of rock, W/(K m).

Eqs. (3), (9), (20), (24) and (28) constitute the gas–solid–thermal coupling model based on the self-diffusive flow model.

2.2. The influence of water absorption and shale creep on the fracture surface

Related studies have shown that the mechanical properties of shale change after water absorption manifested as the decrease in Young's elastic modulus and the increase in Poisson's ratio (Akrad et al., 2011; Das et al., 2014). Akrad et al. (2011) conducted mechanical parameter testing and proppant embedding experiments in Bakken, Barnett, Eagle Ford, and Haynesville shales. The results show that Young's modulus of shale decreases after immersion in fracturing fluid, and both high temperature and carbonate content positively affect the decrease in Young's modulus after immersion in water.

Table 2 shows the elastic modulus test results of shale cores in different regions of the United States before and after immersion by Akrad et al. (2011). It can be found that, due to the different mineral compositions of shale cores in different regions, the reduction degree of elastic modulus varies greatly after immersion. For the shale in the same area, the high temperature increases the loss of the shale elastic modulus after water immersion.

Wang (2015) conducted uniaxial compression experiments under constant confining pressure (15 MPa) to study the effects of moisture content and stress on shale creep. Fig. 1 shows part of Wang's experimental results. Due to the elastic response of shale, initial strain is generated at the initial time. With the increase in water content, the initial strain variable of the core increases, which indicates that the elastic modulus of shale decreases with the increase in water content. With the increase in loading time, shale creep occurs, and the maximum creep of shale increases with the increases in water content and load.

In the fracturing process, the fracture surface is immersed in fracturing fluids, which reduces the elastic modulus of the fracture surface and increases the creep of the fracture surface. Maxwell's model is used to describe the creep of the fracture plane in this paper. Maxwell's model consists of a viscous element and an elastic element in series, both of which bear the same stress, and its strain is the sum of the strains of the viscous element and the elastic element, see Fig. 2. Therefore, the constitutive relation of Maxwell's body can be expressed as

$$\dot{\varepsilon} = \frac{\dot{\sigma}}{E_{\text{s}}} + \frac{\sigma}{\eta} \tag{30}$$

where E_{s} is the elastic modulus of the fracture surface, Pa; η is the creep viscosity coefficient, Pa s.

By integrating the time term of the strain in Eq. (30), the creep equation of Maxwell's model can be expressed as

$$\varepsilon = \frac{1}{\eta}\sigma_0 t + \frac{\sigma_0}{E_{\text{s}}} \tag{31}$$

The equivalent elastic modulus can be obtained from Eq. (31):

$$\tilde{E}_{\text{s}} = \frac{E_{\text{s}}}{1 + E_{\text{s}}t/\eta} \tag{32}$$

As shown in Fig. 3, the fracture surface is soaked with the fracturing fluid during fracturing, which will change the permeability and porosity of the fracture surface. The permeability and porosity near the fracture surface will increase if fracturing fluids induce micro-fractures in the shale matrix and decrease if there is no microfracture.

Suppose there is a transition zone with minimal thickness from shale matrix to fracture surface, whose thickness is h_{t}. Then the

Table 2
Test results of shale elastic modulus before and after water immersion in different areas.

Region	Immersion conditions	Elastic modulus, GPa		Reduction degree, %
		Before immersion	After immersion	
Lower Bakken	Room temperature, 5 days, 2% KCl slickwater	24.18	20.39	15.67
	Room temperature, 30 days, 2% KCl slickwater	47.39	33.85	28.56
	149 °C, 2 days, 2% KCl slickwater	47.39	36.85	22.24
Middle Bakken	Room temperature, 30 days, 2% KCl slickwater	57.38	34.11	40.56
	149 °C, 2 days, 2% KCl slickwater	70.84	33.73	52.39
	149 °C, 2 days, 2% KCl distilled water	74.39	35.73	51.97
Barnett	Room temperature, 5 days, 2% KCl slickwater	45.97	41.35	10.06
	Room temperature, 15 days, 2% KCl slickwater	45.97	38.93	15.32
	Room temperature, 30 days, 2% KCl slickwater	47.22	40.98	13.22
	149 °C, 2 days, 2% KCl slickwater	50.57	34.45	31.88
	149 °C, 2 days, 2% KCl distilled water	74.17	44.05	40.61
Eagle Ford	Room temperature, 5 days, 2% KCl slickwater	35.09	25.18	28.25
	Room temperature, 15 days, 2% KCl slickwater	44.85	21.25	52.63
	Room temperature, 30 days, 2% KCl slickwater	35.09	19.35	44.85
	149 °C, 2 days, 2% KCl slickwater	35.09	10.50	70.08
Haynesville	Room temperature, 5 days, 2% KCl slickwater	38.74	35.79	7.62
	Room temperature, 30 days, 2% KCl slickwater	38.74	36.32	6.29
	149 °C, 2 days, 2% KCl slickwater	38.74	36.41	6.01

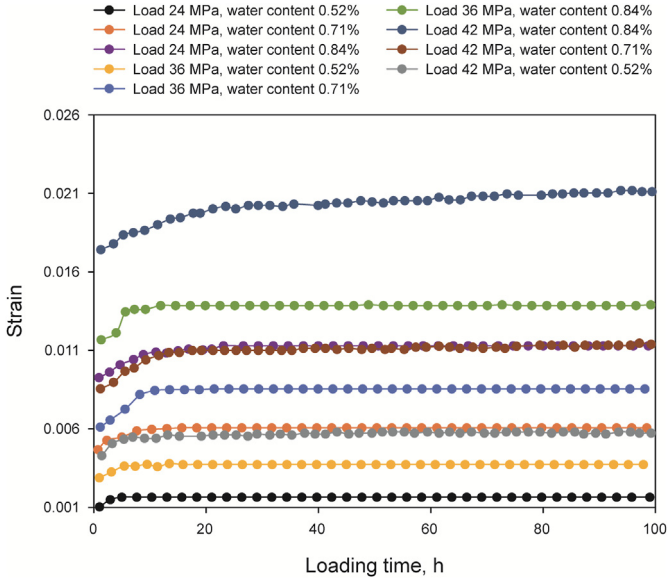

Fig. 1. Creep curves of shale with different loads and water saturation (Wang, 2015).

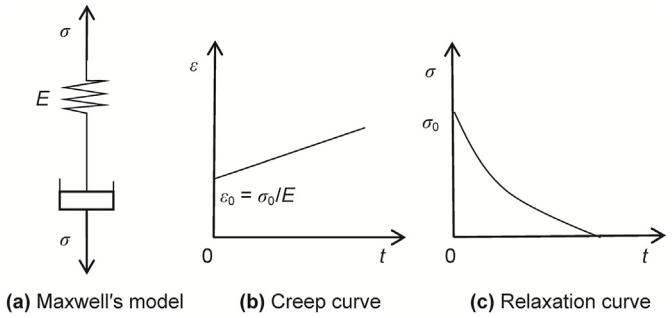

Fig. 2. Maxwell deformation characteristics.

mass flow rate of gas passing through the transition zone is

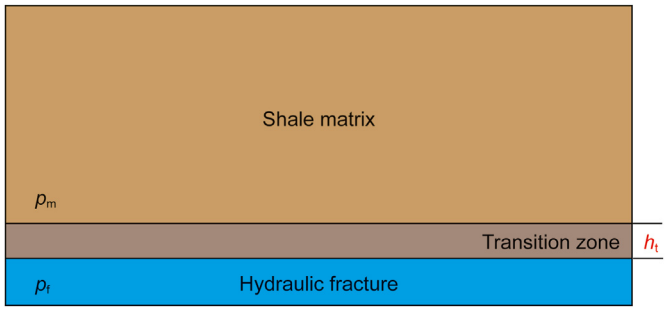

Fig. 3. Shale matrix and fracture after fracturing.

$$v = -D_{\text{eff"TT5843c571""ADt}}\nabla\rho = -\rho_{\text{ga}}D_{\text{eff"TT5843c571""ADt}}Z_{\text{p}}\nabla p \tag{33}$$

When h_{t} is very small, Eq. (33) can be written as

$$v = \rho_{\text{ga}}D_{\text{eff"TT5843c571""ADt}}Z_{\text{p}}\frac{p_{\text{m}} - p_{\text{f}}}{h_{\text{t}}} = \rho_{\text{ga}}R_{\text{b}}\left(p_{\text{m}} - p_{\text{f}}\right) \tag{34}$$

$$R_{\text{b}} = \frac{D_{\text{eff"TT5843c571""ADt}}Z_{\text{p}}}{h_{\text{t}}} \tag{35}$$

where $D_{\text{eff–t}}$ is the self-diffusivity of transition zone, m^2/s; R_{b} is the permeation coefficient of fracture surfaces, m/(s Pa), and it is affected by the fracture surface porosity; p_{m} and p_{f} are the matrix pressure and the fracture pressure, respectively, Pa; and p_{m} is the same to p; h_{t} is the thickness of the transition zone, m.

2.3. The influence of proppants on fracture closure

According to the geometry, the commonly used proppants are divided into spherical proppant and cylindrical proppant. The packing mode of proppant in hydraulic fracture is supposed to be face-centered dense packing, as shown in Fig. 4. For spherical proppants, each proppant is in contact with four (number of layers equal to two) or eight (number of layers greater than two) proppants, and for cylindrical proppants, each proppant is in contact with two (number of layers equal to two) or eight (number of layers greater than two) proppants.

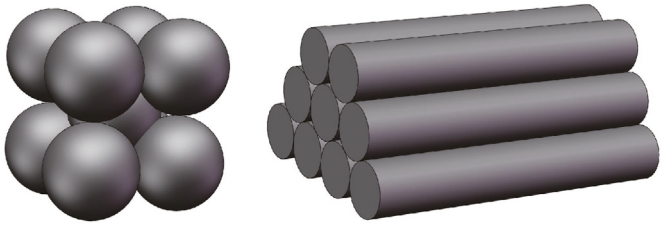

Fig. 4. Proppant accumulation mode.

For the convenience of model derivation, it is assumed that

(1) The proppant is evenly distributed inside the fracture;
(2) The proppant has the same particle size and mechanical properties, and its deformation is elastic;
(3) Neglecting the broken part of the proppant.

Thus, the displacement of fracture surfaces only includes the elastic deformation of proppants and the proppant embedment in the fracture surface, which can be expressed as follows:

$$\Delta w_f = (n-1)\alpha\sin\varphi + 2(\alpha' + h) \tag{36}$$

where n is the number of proppant layers; α is the elastic deformation between proppants, m; α' is the elastic deformation of proppant in the layer in contact with the fracture surface, m; h is the depth of proppant embedded in the layer in contact with the fracture surface, m; φ is the center line angle between proppant in different layers, °. For spherical proppant, $\varphi = 45°$, and for cylindrical proppant, $\varphi = 60°$.

Based on Hertz contact theory (Johnson, 1987), the elastic deformation between two forward contact spherical particles shown in Fig. 5 is (Puttock and Thwaite, 1969)

$$\alpha = \frac{(3\pi)^{2/3}}{2} F^{2/3} \cdot (V_1 + V_2)^{2/3} \cdot \left(\frac{1}{d_1} + \frac{1}{d_2}\right)^{1/3} \tag{37}$$

$$V_1 = \frac{1-\nu_1^2}{\pi E_1} \tag{38}$$

$$V_2 = \frac{1-\nu_2^2}{\pi E_2} \tag{39}$$

where α is the elastic deformation of spherical particles, m; F is the force exerted on a spherical particle, N; d_1 and d_2 are spherical particle diameters, m; E_1 and E_2 are the Young's modulus of two spherical particles, MPa; ν_1 and ν_2 are Poisson's ratios of two spherical particles.

Fig. 6 shows the contact mode of spherical proppant inside the fracture. The force decomposition relationship is as follows:

$$F' = F \Big/ \sqrt{3} \tag{40}$$

The force acting on a single proppant is

$$F' = A_p \sigma_{eff} = \frac{\pi d_p^2 \sigma_{eff}}{4\sqrt{3}} \tag{41}$$

where A_p is the central section area of proppant, m^2; σ_{eff} is the fracture closure stress, MPa; d_p is the proppant diameter, m.

By substituting Eqs. (40) and (41) into Eq. (37), the elastic deformation between two spherical proppant layers in the fracture can be obtained

$$\alpha_d = \frac{(3\pi)^{2/3}}{2} \left(\frac{\pi d_p^2 \sigma_{eff}}{4\sqrt{3}}\right)^{2/3} \cdot (2V_p)^{2/3} \cdot \left(\frac{2}{d_p}\right)^{1/3} \tag{42}$$

$$V_p = \frac{1-\nu_p^2}{\pi E_p} \tag{43}$$

where E_p is the elastic modulus of proppants, MPa; ν_p is Poisson's ratio of proppants.

As shown in Fig. 7, the fracture plane can be regarded as spherical particles with infinite radius, but the creep of the fracture surface needs to be considered. Therefore, the sum of the elastic deformation of the proppant in contact with the fracture surface and the proppant embedment in the fracture surface is

$$\alpha' + h = \frac{d_p}{2} \cdot \left\{ \frac{3\pi\sigma_{eff}}{4\left[\frac{1}{\left(1-\nu_p^2\right)\Big/E_p + \left(1-\nu_s^2\right)\Big/\tilde{E}_s}\right]} \right\}^{2/3} \tag{44}$$

$$V_s = \frac{1-\nu_s^2}{\pi \tilde{E}_s} \tag{45}$$

where $\tilde{E}_s$ is the elastic modulus of the fracture plane after creep is considered, MPa; ν_s is Poisson's ratio of the fracture plane.

Assuming that the elastic modulus of the fracture surface is infinite, that is, the fracture surface will not be deformed, the deformation of the proppant layer in contact with the fracture plane can be obtained from Eq. (42) as follows:

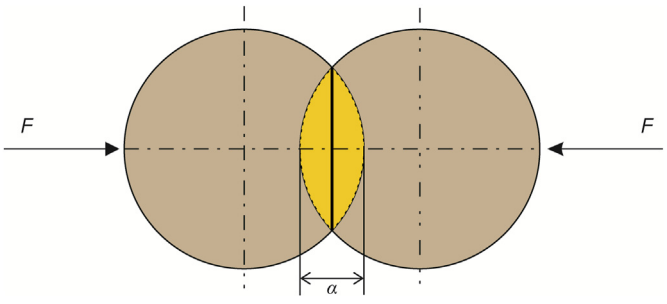

Fig. 5. Forward contact of spherical particles.

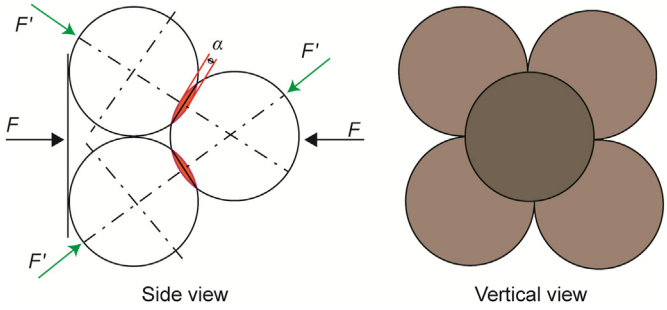

Fig. 6. Contact mode of spherical proppant.

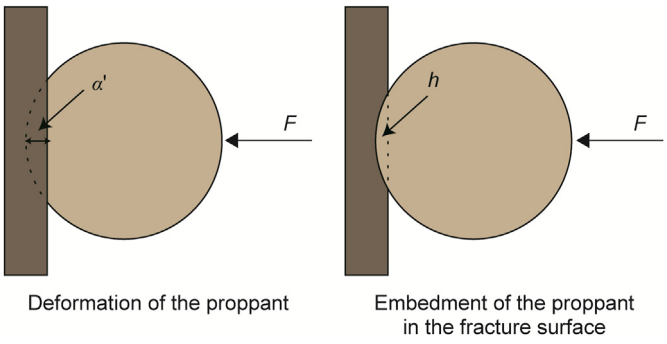

Fig. 7. Interaction between proppant and fracture surface.

$$\alpha' = \frac{(3\pi)^{2/3}}{2}\left(\frac{\pi d_p^2 \sigma_{eff}}{4\sqrt{3}}\right)^{2/3} \cdot V_p^{2/3} \cdot \left(\frac{1}{d_p}\right)^{1/3} \tag{46}$$

Therefore, the proppant embedment depth in the fracture plane is obtained through Eqs. (44)–(46):

$$h = \frac{(3\pi)^{2/3}}{2}\left(\frac{\pi d_p^2 \sigma_{eff}}{4\sqrt{3}}\right)^{2/3} \cdot \left[(V_p + V_s)^{2/3} - V_p^{2/3}\right] \cdot \left(\frac{1}{d_p}\right)^{1/3} \tag{47}$$

Based on Hertz contact theory (Puttock and Thwaite, 1969), following the above derivation process from Eq. (37) to Eq. (47), we can get the formulation of the embedment of cylindrical proppant:

$$\alpha_d = \sqrt{2} d_p \sigma_{eff} V_p \cdot \left[1 + \ln\left(\frac{2\sqrt{2} l_p^2}{d_p^2 \sigma_{eff} V_p}\right)\right] \tag{48}$$

$$\alpha' = \frac{d_p \sigma_{eff}}{\sqrt{2}} V_p \cdot \left\{1 + \ln\left[\frac{2\sqrt{2} l_p^2}{d_p^2 \sigma_{eff} V_p}\right]\right\} \tag{49}$$

$$h = \frac{d_p \sigma_{eff}}{\sqrt{2}} \cdot \left\{(V_p + V_s) \cdot \left[1 + \ln\left(\frac{2\sqrt{2} l_p^2}{d_p^2 \sigma_{eff}(V_p + V_s)}\right)\right] - V_p \cdot \left[1 + \ln\left(\frac{2\sqrt{2} l_p^2}{d_p^2 \sigma_{eff} V_p}\right)\right]\right\} \tag{50}$$

2.4. The influence of proppants on mass transfer between rock matrix and fractures

When gas flows from the shale matrix into the fracture, the embedded proppant acts as a "plug" to block the pores on the fracture surface, as shown in Fig. 8. When the fracture closure stress is 0, the proppant is not embedded, and the contact between the proppant and the fracture surface is point contact. At this time, the effective drainage surface area of the fracture is maximum. As the production time goes on, the embedment of the proppant will decrease the fracture surface porosity, thus decreasing the permeation coefficient of the fracture surface.

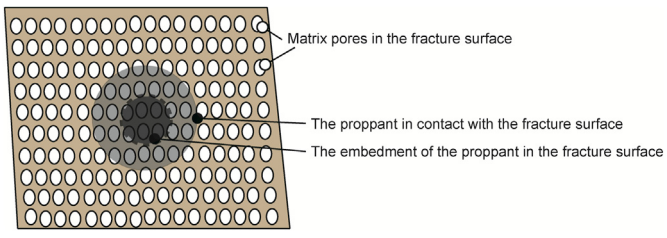

Fig. 8. The proppant on the fracture surface is embedded to block the matrix hole.

2.4.1. Spherical proppant

As seen in Fig. 9, the area of the embedded part of the spherical proppant is

$$S_{em} = \pi\left[R^2 - (R-h)^2\right] \tag{51}$$

where h is the proppant embedding depth, mm; R is the proppant radius, mm.

Therefore, the ratio of the embedded area of the proppant to the central section area of the proppant is as follows:

$$rat_{em} = \frac{S_{em}}{S_{em} + S_{ou}} = \frac{R^2 - (R-h)^2}{R^2} = 1 - \left(1 - \frac{h}{R}\right)^2 \tag{52}$$

where S_{em} and S_{ou} are respectively the embedded area of the proppant and the central section area of the proppant.

There is still an area that cannot be covered by the proppant. The lateral view of the first proppant layer on the fracture surface is shown in Fig. 10. Then

$$S_2 = S_3 = S_4 = \frac{\pi R^2}{6} \tag{53}$$

$$S_1 = \sqrt{3}R^2 - S_2 - S_3 - S_4 = \left(\sqrt{3} - \frac{1}{2}\right)R^2 \tag{54}$$

Therefore, the area coverage of proppant on the fracture plane is

$$rat_{ov} = \frac{S_2 + S_3 + S_4}{S_1 + S_2 + S_3 + S_4} = \frac{\pi R^2 / 2}{\sqrt{3}R^2} = \frac{\pi}{2\sqrt{3}} \tag{55}$$

Assuming that the elastic deformation of the proppant has little effect on its radius, S_i (i = 1–4) in Fig. 10 does not change with proppant embedment. So, the proportion of proppant embedding area in the total fracture area is

$$rat_{ha} = rat_{em} \times rat_{ov} = \frac{\pi}{2\sqrt{3}}\left[1 - \left(1 - \frac{h}{R}\right)^2\right] \tag{56}$$

The spherical proppant embedment can be calculated with Eq. (47).

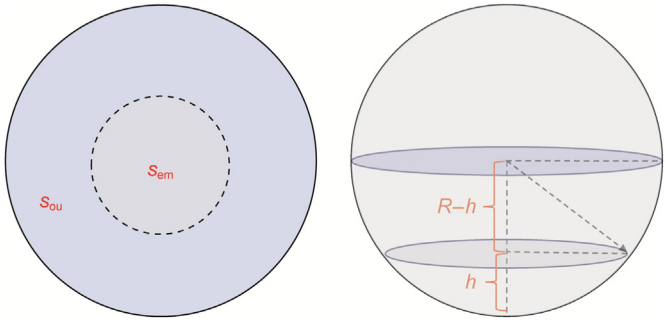

Fig. 9. Single spherical proppant embedded in top and side views.

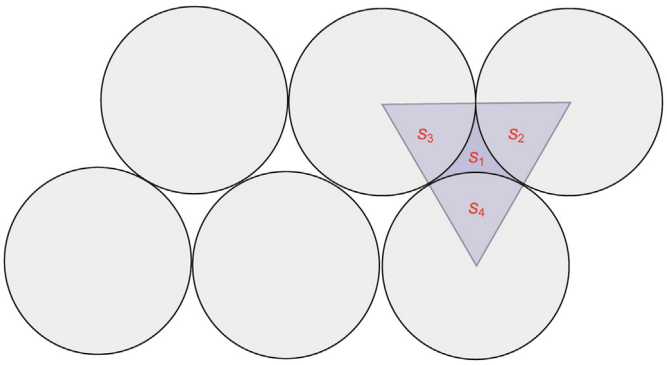

Fig. 10. Top view of spherical proppant laid on crack surface.

2.4.2. Cylindrical proppant

Fig. 11 shows that the area of the embedded part of the cylindrical proppant is

$$S_{em} = 2l_p\sqrt{R^2 - (R-h)^2} \tag{57}$$

where l_p is the column proppant length, mm; R is the cylindrical proppant radius, mm.

Therefore, for the area covered by a single proppant, the ratio of the embedded area to the central section area of the proppant is

$$rat_{em} = \frac{S_{em}}{2Rl_p} = \sqrt{1 - \left(1 - \frac{h}{R}\right)^2} \tag{58}$$

When the proppant is closely laid on the fracture surface, the frontal view of the proppant on the fracture surface is shown in Fig. 12. Therefore, considering that proppants cover the entire fracture surface, the proportion of proppant embedding area occupying the total fracture area is

$$rat_{ha} = rat_{em} = \sqrt{1 - \left(1 - \frac{h}{R}\right)^2} \tag{59}$$

Assuming that gas cannot enter the fracture from the fracture surface area where proppant is embedded, the relationship between the effective drainage surface area of the fracture and proppant embedment can be expressed as follows:

$$R_b = R_{b0}(1 - rat_{ha}) = \frac{D_{eff}Z_p}{h_t}(1 - rat_{ha}) \tag{60}$$

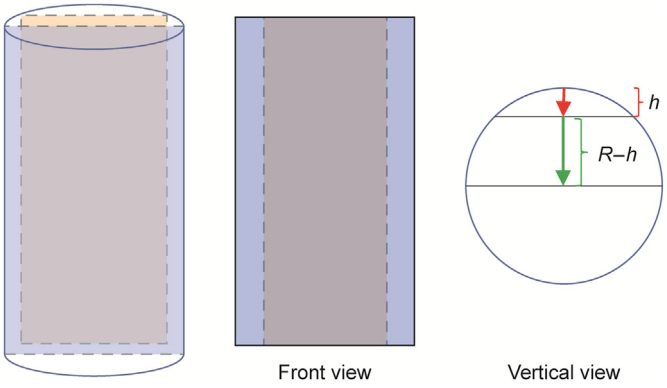

Fig. 11. Single cylindrical proppant embedded in top and side views.

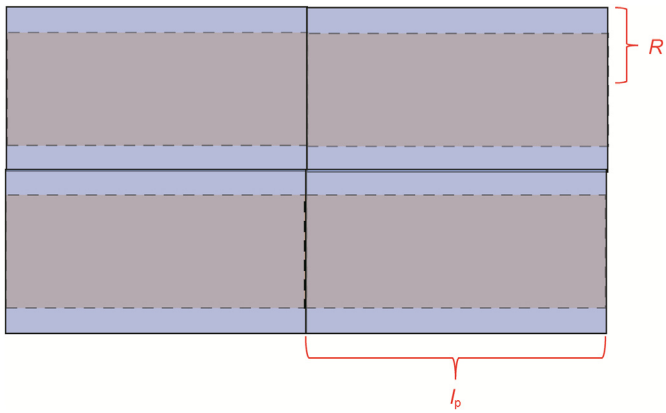

Fig. 12. Front view of cylindrical proppant on fracture surface.

Whether it is a spherical proppant or cylindrical proppant, it only needs to substitute the corresponding value into Eq. (60) to calculate the effect of proppant embedding on the mass transfer between rock matrix and fractures. In Eq. (60), the thickness of the transition zone of the matrix to fracture, h_t, is influenced by fracturing fluid invasion. Therefore, Eq. (60) reflects the influence of fracturing fluid invasion and the proppant embedment on the mass transfer rate between fractures and rock matrix.

3. Discontinuous finite element method

The left figure of Fig. 13 shows the actual fracture schematic diagram. The middle figure of Fig. 13 compares the discrete fracture model and the discontinuous discrete fracture model (Wei et al., 2021), and the right figure compares the mesh generation results of the discrete fracture model (DFM) and the discontinuous discrete fracture model (DDFM). DDFM is modified from DFM, which aims to solve the following 3 problems: 1) Considering the influence of the fracture surface on the mass transfer rate between fracture and matrix. 2) Considering the displacement discontinuity of fracture surfaces. The fracture node in the numerical calculation of DFM is also the matrix node. At the same time, the finite element method is a continuous interpolation calculation method, so the calculated solid displacement is continuous at the fracture. Thus, it is impossible to calculate the closure displacement of the propped fracture directly. 3) Considering the actual morphology of fractures. Since the realistic fracture width changes from its center to the tip, the displacement required for complete closure of the fracture at different positions is different. Therefore, it is essential to consider the fracture morphology. DDFM developed in this section solves the three disadvantages of DFM while retaining the advantages of the discrete fracture model.

3.1. Coupling flow between the matrix pores and discrete fractures

In Fig. 13, Ω_m and Ω_f are the matrix region and the fracture region, respectively, Γ_f^+ and Γ_f^- are the upper and lower surfaces of the fracture, respectively. According to Eq. (34), the mass transfer through the upper and lower fracture surfaces can be expressed as

$$v^+ = \rho_{ga}R_b\left(p_m - p_f\right)\cdot\boldsymbol{n}_f^+ \tag{61}$$

$$v^- = \rho_{ga}R_b\left(p_m - p_f\right)\cdot\boldsymbol{n}_f^- \tag{62}$$

The governing equation of matrix flow considering fluid–solid

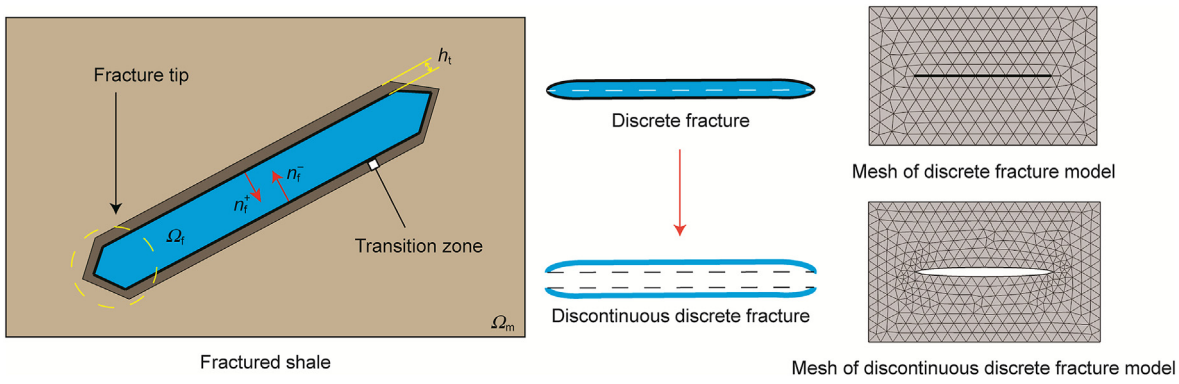

Fig. 13. Comparison between discrete fracture and discontinuous discrete fracture.

coupling can be written as follows:

$$\rho_{ga}\phi(c_s+Z_p)\frac{\partial p}{\partial t}+\rho_{ga}(\alpha-\phi)\frac{\partial \varepsilon_v}{\partial t}-\nabla\cdot\left(\rho_{ga}Z_pD_{eff}\nabla p\right)=v^+\cdot\boldsymbol{n}_f^+ + v^-\cdot\boldsymbol{n}_f^- \tag{63}$$

According to Biot's theory of pore-elasticity (Chen and Teufel, 1997), we have

$$\frac{\partial \varepsilon_v}{\partial t}=\frac{\alpha}{3K}\frac{\partial p}{\partial t} \tag{64}$$

where α is the effective stress coefficient; K is the matrix bulk modulus, MPa.

Substituting Eq. (64) into Eq. (63), the matrix flow governing equation can be written as follows:

$$\rho_{ga}\left[\phi(c_s+Z_p)+\frac{\alpha(\alpha-\phi)}{3K}\right]\frac{\partial p}{\partial t}-\nabla\cdot\left(\rho_{ga}Z_pD_{eff}\nabla p\right)=v^+\cdot\boldsymbol{n}_f^+ + v^-\cdot\boldsymbol{n}_f^- \tag{65}$$

The weak form of Eq. (65) is

$$\rho_{ga}\phi\left(c_s+Z_p+\frac{\alpha(\alpha-\phi)}{3K}\right)\int_{\Omega_m}\delta p\frac{\partial p}{\partial t}\mathrm{d}\Omega-\int_{\Omega_m}\left[\delta p\nabla\cdot\left(\rho_{ga}Z_pD_{eff}\nabla p\right)\right]\mathrm{d}\Omega=-\rho_{ga}R_bh_t\int_{\Gamma_f^+ +\Gamma_f^-}\delta p\left(p_m-p_f\right)\mathrm{d}\Gamma \tag{66}$$

The weak form of the flow governing equation for each fracture surface is

$$w_f\times\int_{\Gamma_f^+}\delta p_f\left[\rho_{ga}\phi_fZ_p\frac{\partial p_f}{\partial t}-\nabla\cdot\left(\rho_{ga}Z_pD_{eff}\nabla p_f\right)\right]\mathrm{d}\Gamma=\rho_{ga}R_bh_t\int_{\Gamma_f^+}\delta p_f\left(p_m-p_f\right)\mathrm{d}\Gamma \tag{67}$$

$$w_f\times\int_{\Gamma_f^-}\delta p_f\left[\rho_{ga}\varphi_fZ_p\frac{\partial p_f}{\partial t}-\nabla\cdot\left(\rho_{ga}Z_pD_{eff-f}\nabla p_f\right)\right]\times\mathrm{d}\Gamma=\rho_{ga}R_bh_t\int_{\Gamma_f^-}\delta p_f\left(p_m-p_f\right)\mathrm{d}\Gamma \tag{68}$$

To consider the influence of fracture surface properties on the mass transfer between the fracture and matrix, different from DFM (Wei et al., 2019), DDFM will not add Eqs. (66)–(68) together during numerical calculation. It is the reason why different pressure symbols (p_m is the pressure in the matrix and p_f is the pressure in the fracture) are used to distinguish the flow equation in the matrix from the flow equation in the fracture.

For the jointed fractures shown in Fig. 14, there will be pressure discontinuity in the joint of each fracture. The reason is that the flow in the same fracture is interrupted at the joint. A flow node is added at the joint to solve the problem of discontinuous flow of fractures at the joint, as shown in Fig. 15. Eq. (69) gives the mass conservation equation at the point.

$$\nabla\cdot\boldsymbol{v}_f=\nabla\cdot\left(-\rho_{ga}Z_pD_{eff}{}^{TT5843c571}{}^{ADf}\nabla p_f\right)=0 \tag{69}$$

As shown in Fig. 15, using finite element method, the numerical discretization scheme of Eq. (69) can be easily assembled with the numerical discretization schemes of Eqs. (66)–(68), as shown in Fig. 16.

3.2. Fracture closure

For the initially open fracture, the mesh generation result is shown in Fig. 17. For the same fracture, the fracture nodes of its two surfaces correspond individually. Therefore, the initial aperture of the fracture can be expressed as

$$w_f^{(0)}=(\boldsymbol{x}_B-\boldsymbol{x}_A)\cdot\boldsymbol{n}_A \tag{70}$$

where $w_f^{(0)}$ is the fracture width of the initial calculation step, m; $\boldsymbol{x}_A$ and $\boldsymbol{x}_B$ are the coordinates of the corresponding fracture nodes.

The fracture aperture considering closure can be calculated by Eq. (36):

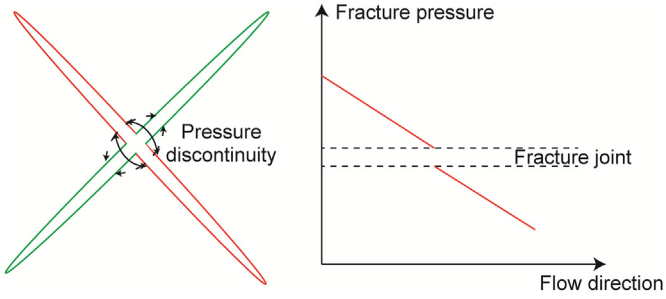

Fig. 14. Cross crack and its internal pressure distribution.

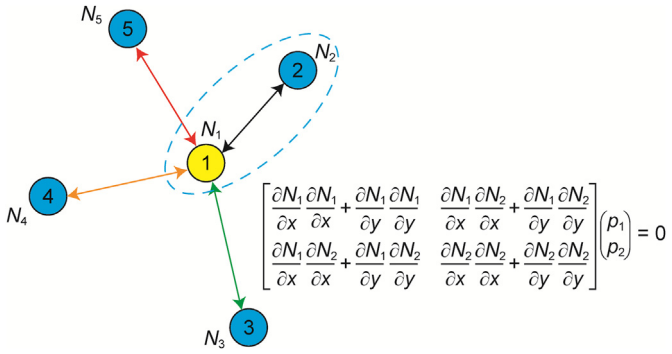

Fig. 15. Calculation of flow distribution at the joint.

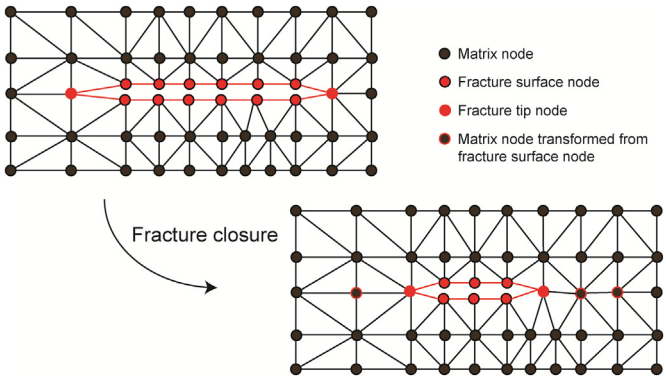

Fig. 17. Node changes during crack closure.

$$w_f^{(n)} = w_f^{(n-1)} - \Delta w_f \tag{71}$$

where $w_f^{(n)}$ and $w_f^{(n-1)}$ are the fracture widths of the nth and $(n-1)$th time steps, respectively, m. When $w_f^{(n)} \le 0$, the fracture is completely closed. As can be seen from Fig. 17, each pair of the fracture surface nodes merges into one matrix node, which approximates the mechanical behavior of the completely closed fracture to that of the matrix.

3.3. Model verification

There are three innovations of DDFM compared with DFM.

(1) Characterize the topology of the fracture.
(2) Quantify the change in the fracture surface area.
(3) Capture the discontinuous displacement of solid in fracture surfaces and the stress concentration in fracture tips.

An actual fracture, shown in Fig. 18, is built to verify the three innovations above of DDFM. The fracture has the same dimension as the rock matrix for the actual fracture model. Moreover, the fracture flow is described using the N–S model. To make this paper as concise as possible, readers can refer to Wei et al. (2022). Fig. 19 shows the difference of the mesh between the actual fracture model and DDFM.

Nonflow boundary and fixed displacement boundary are applied to the outer boundary:

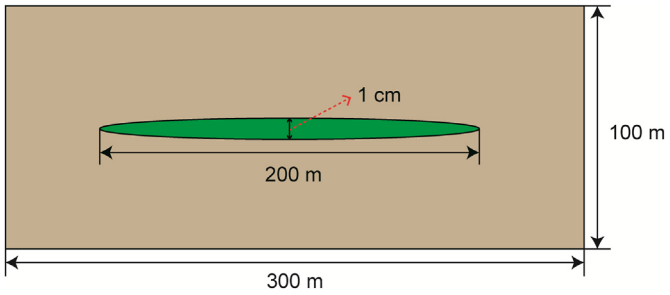

Fig. 18. Geometry model of single fracture.

$$\nabla p \cdot \boldsymbol{n} = 0, \quad u = 0 \tag{72}$$

The middle point of the fracture is set as the constant pressure boundary:

$$p = p_h \tag{73}$$

The fracture surface is set as the positioning displacement boundary, and the displacement was calculated by the stress on the fracture surface using Eq. (36). In this section, only the spherical proppant support was considered.

Fig. 20 shows the simulation results of pore pressure using

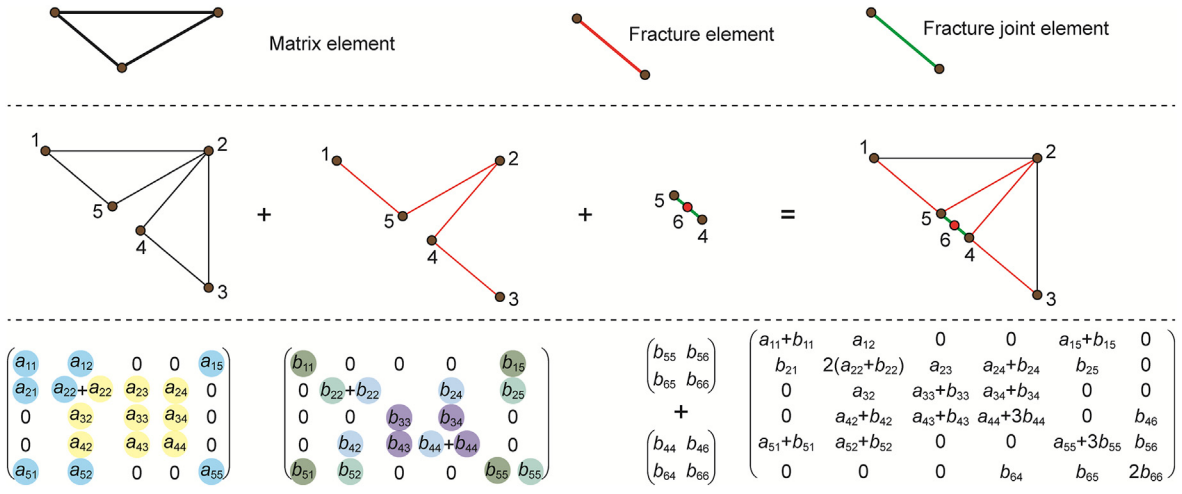

Fig. 16. Matrix assembly for numerical calculation of DDFM.

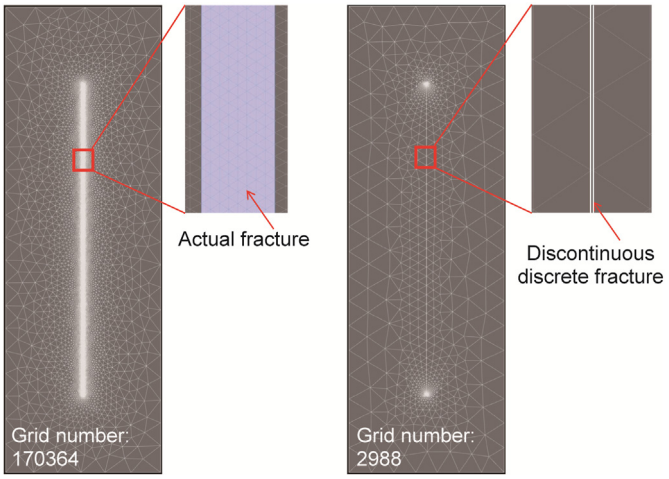

Fig. 19. Mesh of the actual fracture model (left) and DDFM (right).

DDFM and the actual fracture model. It can be seen from the middle figure and the right figure that the fracture closure degree of the DDFM is slightly greater than that of the actual fracture model. The reason is that when the real fracture flow space is established, the fracture space needs to be divided into grids, and the grid inside the fracture also has a specific stiffness, increasing the support effect on the fracture surface. Therefore, the fracture closure calculated by the actual fracture model is smaller than that of DDFM, as shown in Fig. 21.

4. Result analysis

4.1. Closure of fracture networks and its influence on shale gas production

In this chapter, a random complex fracture network is established. Each fracture is an ellipsoid in 3D space, as shown in Fig. 22. The initial maximum width of the primary fracture is 1 cm, and the initial maximum width of the secondary fracture is 5 mm. The height of the primary fracture is 60 m and the length is 200 m. The height of the secondary fractures is from 25 to 50 m, and the length

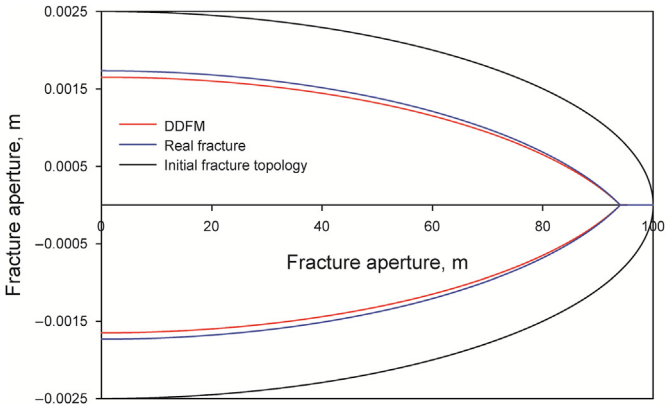

Fig. 21. Comparison of fracture aperture after 300 days of production.

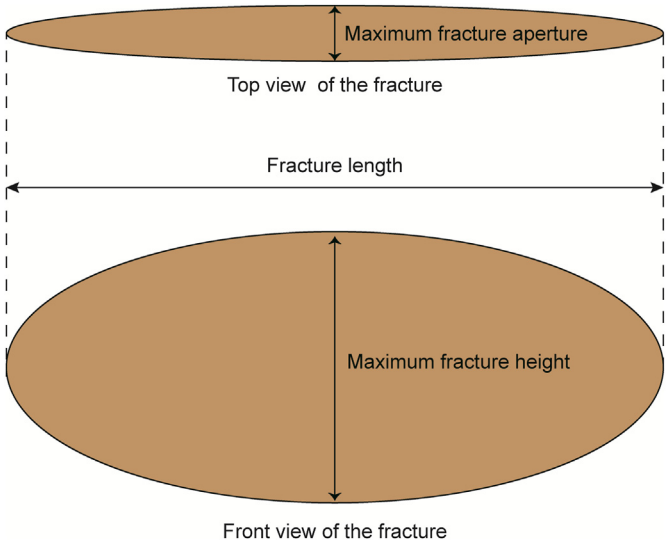

Fig. 22. 3-dimensional geometry model of single fracture.

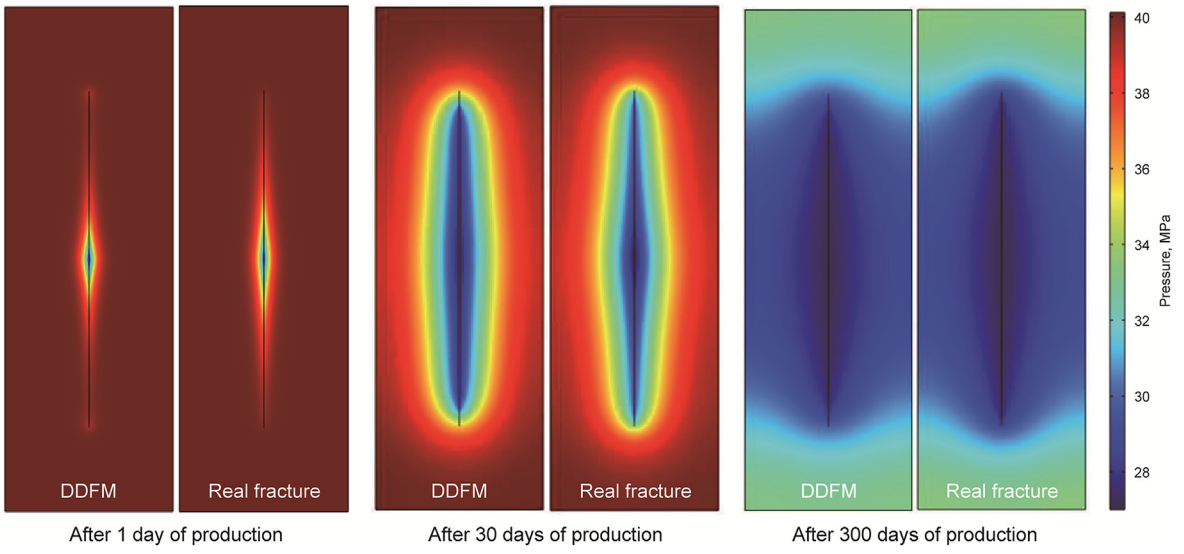

Fig. 20. Pressure comparison after different production time.

is from 40 to 100 m. The minimum horizontal principal stress is along the x axis and perpendicular to the primary fracture. The maximum horizontal principal stress is along the y axis. The overburden stress $S_v = 55$ MPa is along the z axis. The outer boundary of the geometry model in Fig. 22 is nonflow boundary and fixed displacement boundary, shown in Eq. (72). The middle point of the primary fracture is set as the constant pressure boundary, i.e., Eq. (73). Fig. 23 shows the geometric model of the complex fracture network used in this chapter, and the basic simulation parameters are listed in Table 3.

It can be seen from Fig. 24 that the fracture aperture decreases with production time, which reduces the effective length and height of fractures. The primary fracture has a larger initial width and is filled with more layers of proppants. Therefore, the primary fracture maintains a larger aperture than the secondary fractures.

Existing studies only consider the adverse impact of fracture closure on production, including decreased fracture aperture, length and height. Because the proppant embedding will block the pores on the fracture surface, thus reducing the fracture surface porosity, i.e., reducing the mass transfer rate between the matrix and the fracture. Besides the fracture closure, DDFM also considers the adverse effect of proppant embedment on production by reducing fracture surface porosity. As seen from Fig. 25, the dimensionless permeation coefficient of fracture surfaces, i.e., R_b/R_{b0}, continuously decreases during the production process. The dimensionless permeation coefficient of fracture surfaces reaches the minimum value, decreasing to 0.2, after one year of production.

In Fig. 26, as production time goes on, the pressure drop inside the fracture gradually expands from the primary fracture to the secondary fracture, which indicates that more fractures begin to play the role of gas transportation. It is also why gas production keeps rising in the early production stage (see Figs. 27 and 28).

The impact of shale creep on gas production is analyzed by fixing the bottom hole pressure. From Fig. 27, the accumulated production considering creep is reduced by 15.2% in one year and 30.8% in three years. The main reason is that shale creep increases the proppant embedment in the fracture surface, reduces the fracture aperture, lowers the effective fracture length and height, and brings down the porosity of the fracture surface. The impacts of fracture closure and surface porosity are analyzed in Fig. 28, which shows that the damage of the fracture surface porosity (or surface permeation coefficient) has a more significant impact on production than fracture closure. When only fracture closure is considered, the accumulated production decreases by 12.7% in one year and 18.1% in three years. When the fracture closure and the fracture surface porosity damage are taken into account, the accumulate production decreases by 32.8% in one year and 42.8% in three years.

4.2. The influence of shale creep on fracture closure and shale gas production

The fracture surface is immersed in fracturing fluid during the hydraulic fracturing process, thus having a higher water content than the shale matrix. The creep viscosity coefficient of the fracture surface will be smaller than that of the rock matrix. In this section, only the creep viscosity coefficient of the fracture surface is changed to study the influence of shale creep on fracture closure and shale gas production without changing its elastic modulus. Three scenarios of the creep viscosity coefficient of the fracture surface are investigated: 1×10^{15}, 1×10^{16}, and 1×10^{17} Pa s. The smaller the creep viscosity coefficient, the stronger the creep property of the fracture surface.

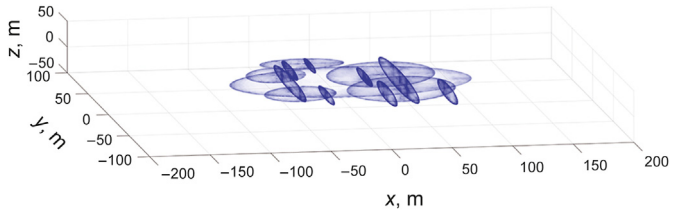

Fig. 23. 3-dimensional geometry model of complex fracture network.

Table 3
Simulation parameters.

Simulation parameter	Value
Thermal conductivity of the rock k_s, W/(K m)	3.29
Thermal conductivity of the gas k_g, W/(K m)	0.14
Heat conductivity β_T, $m^2/(s\ K)$	3×10^{-11}
Specific heat capacity of the rock C_s, kJ/(kg K)	0.937
Specific heat capacity of CH_4 C_g, kJ/(kg K)	2.227
Interstitial convective heat transfer coefficient q_{sf}, W/(m^3 K)	1000
Effective stress coefficient α	0.8
Elasticity modulus of the rock E, GPa	25
Poisson's ratio of the rock v	0.23
Creep viscosity coefficient of the rock η, Pa s	1×10^{17}
Elasticity modulus of the fracture surface E_s, GPa	12
Poisson's ratio of the fracture surface v_s	0.2
Creep viscosity coefficient of the fracture surface η_s, Pa s	1.6×10^{16}
Desorption rate of adsorbed gas k_d, 1/s	1×10^{-5}
Adsorption rate of free gas k_a, 1/s	1×10^{-6}
Langmuir strain constant ε_L	2.72×10^{-3}
Gas viscosity μ, Pa s	3×10^{-5}
Initial pore pressure p_0, MPa	40.12
Critical pressure of CH_4 p_c, MPa	4.539
Critical temperature of CH_4 T_c, K	190.7
Bottom hole pressure p_h, MPa	27
Langmuir pressure of CH_4 p_L, MPa	4.48
Rock density ρ_s, kg/m^3	2500
Minimum horizontal principal stress S_h, MPa	47.3
Maximum horizontal principal stress S_H, MPa	50.6
Initial formation temperature T_0, K	429.15
Elasticity modulus of the proppant E_p, GPa	5
Poisson's ratio of the proppant v_p	0.23
Number of proppant layers n	5
Thickness of Tthetransition zone in fracture surfaces h_t, m	0.05

As seen in Fig. 29, the fracture aperture increases significantly with the increase in the creep viscosity coefficient of the fracture surface, especially for secondary fractures. Fig. 30 shows the impact of the creep viscosity coefficient of the fracture surface on the dimensionless permeation coefficient of fracture surfaces after 1 year of production. As seen in Fig. 30, the average values of the dimensionless permeation coefficient of fracture surfaces increase up to 0.3 and 0.75 when the creep viscosity coefficient of the fracture surface increases from 1×10^{15} to 1×10^{16} and 1×10^{17} Pa s.

It is known that a larger creep viscosity coefficient indicates more prominent creep characteristics of shale. Fig. 31 shows that the gas production rate and the accumulated gas production decrease significantly with the decline of the creep viscosity coefficient of fracture surfaces (i.e., the creep property of shale is enhanced). The accumulated gas production of 900 days decreases up to 12.9% and 50.1% when the creep viscosity coefficient of fracture surfaces decreases from 1×10^{17} to 1×10^{16} and 1×10^{15} Pa s. As the laboratory results shown in Fig. 1, the increase in water saturation will enhance the creep property of shale, i.e., the larger the water saturation in shale, the smaller the creep viscosity coefficient of fracture surfaces. Therefore, understanding the creep properties of shale after fracturing is essential to predict fracture closure and shale gas production.

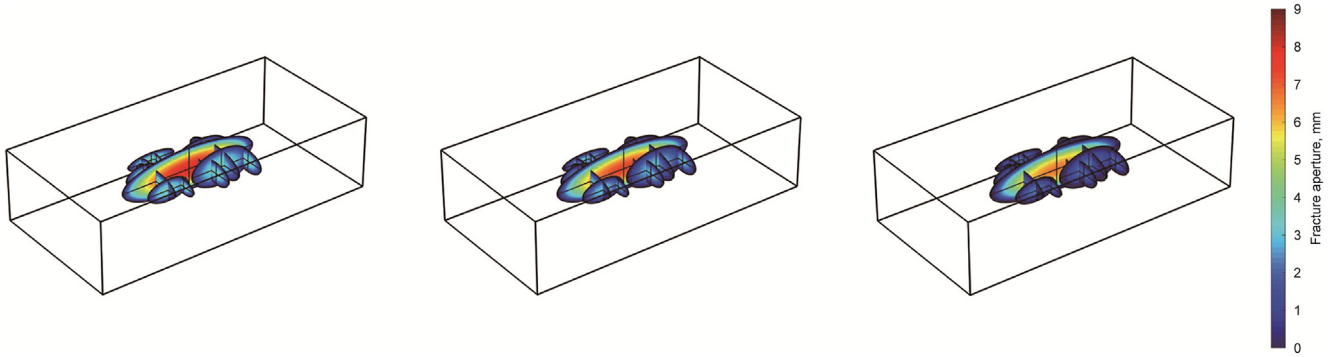

Fig. 24. Fracture aperture change during production (left: 1 month; middle: half year; right: 1 year).

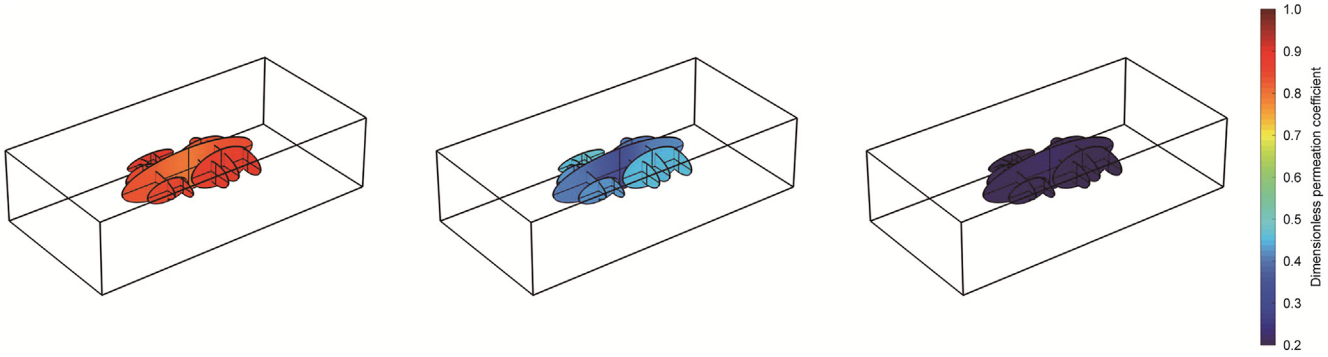

Fig. 25. Dimensionless permeation coefficient of fracture surfaces (R_b/R_{b0}) change during production (left: 1 month; middle: half year; right: 1 year).

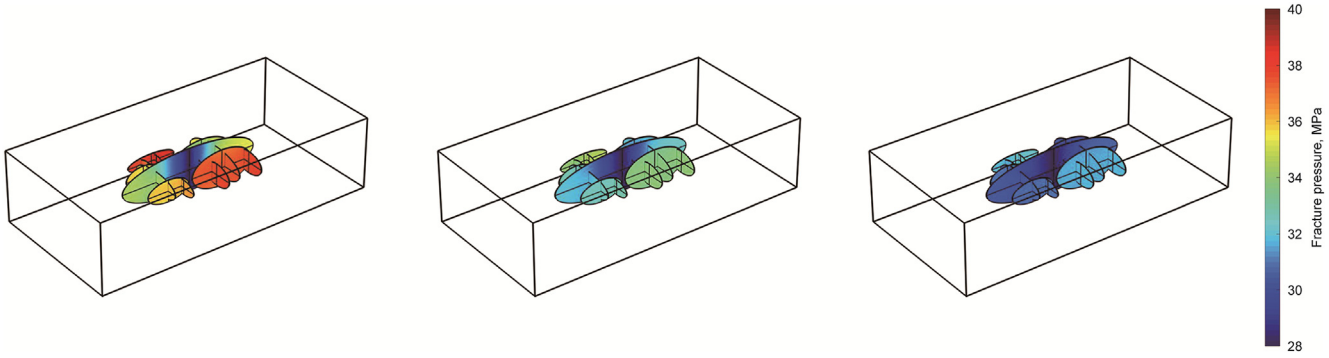

Fig. 26. Fracture pressure change during production (left: 1 month; middle: half year; right: 1 year).

4.3. The influence of initial formation temperature on fracture closure and shale gas production

The formation temperature has a significant influence on the bulk viscosity of CH_4, which has a significant influence on the diffusion coefficient of shale gas. In addition, the rise of formation temperature accelerates the desorption rate of adsorbed gas. In this section, different initial formation temperatures are changed to study the impact of formation temperature changes on fracture closure and shale gas production at a given bottom hole temperature (333 K).

Fig. 32 shows that the fracture aperture increases slightly with the initial formation temperature increasing. On the one hand, as the initial formation temperature increases, the difference between bottom hole temperature and formation temperature increases, leading to greater thermal stain, i.e., shrinkage of the shale matrix. On the other hand, with the increase in temperature difference, the desorption rate of adsorbed gas will be higher, which will increase the shrinkage of the shale matrix.

In Fig. 33, the shale gas production rate decreases with the increase in initial formation temperature. According to the relationship between the volume viscosity of methane and temperature in Fig. 34, μ_b (370 K) > μ_b (400 K) > μ_b (430 K), and the bulk viscosity (μ_b) of CH_4 is much larger than its shear viscosity. Therefore, the diffusion coefficient of CH_4 is reversely related to the formation temperature. The gas flow capacity is enhanced with the increase in

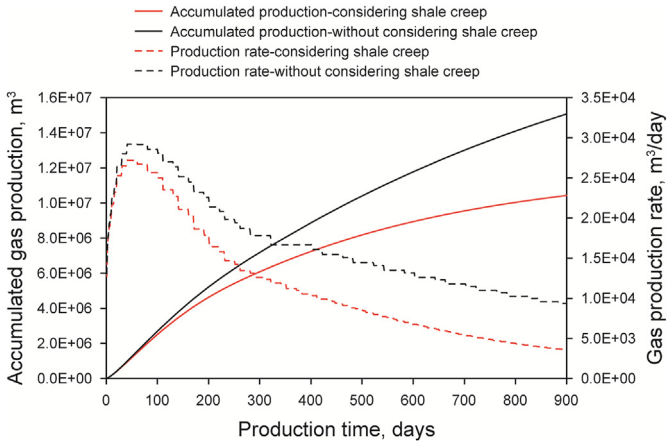

Fig. 27. Effect of shale creep on gas production.

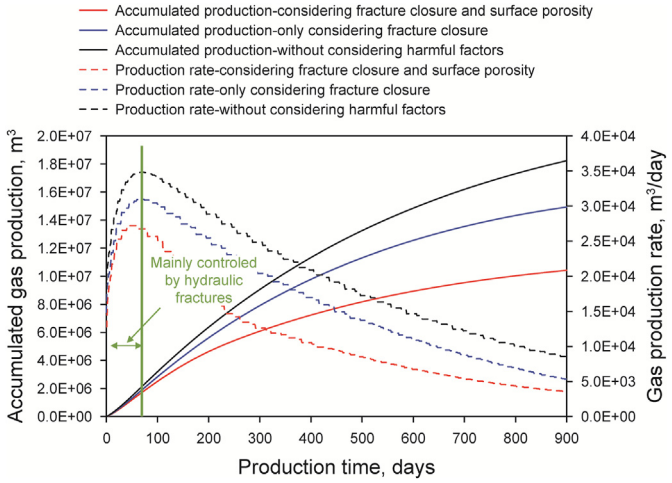

Fig. 28. Effect of fracture closure and surface porosity on gas production.

the initial formation temperature. The formation pressure distribution in the middle section is shown in Fig. 35. The formation pressure near the fracture drops with the increase in the initial formation temperature.

4.4. The influence of proppant type on fracture closure and shale gas production

This section compares the supporting effects of spherical proppant and cylindrical proppant under the same degree of placement inside the fracture. The diameter and mechanical properties of different types of proppants are the same, and the length of a cylindrical proppant is 2, 4, and 6 times its diameter, respectively.

As can be seen from Fig. 36, the aperture of cylindrical proppant propped fractures is close to that of spherical proppant propped fractures. According to the cubic law of fracture conductivity, the fracture conductivity is linear related to the cubic of fracture aperture, which means that the fracture conductivity of the four scenarios in Fig. 36 is almost the same. Fig. 37 represents the dimensionless permeation coefficient of fracture surfaces after 1-year production. The dimensionless permeation coefficient of the cylindrical proppant propped fracture surface is higher than that of the cylindrical proppant propped fracture surface. And the smaller the ratio of the proppant length to its diameter, the higher the dimensionless permeation coefficient of the fracture surface. As stated in Section 2.4, the embedment of the proppants will reduce the mass transfer rate between the fracture and the matrix. The spherical proppant is in point contact with the fracture surface, while the cylindrical proppant is in linear contact with the fracture surface. Therefore, the embedment of the cylindrical proppant is smaller than the spherical proppant.

Fig. 38 shows that the gas production rate of the four scenarios differentiates after 30 days of production. And the production rate of the cylindrical proppant propped fracture is higher than that of the spherical proppant propped fracture. When the cylindrical proppant with $l_p = 2d_p$ is used, the accumulated gas production of 900 days is the highest and is 12.2% higher than that when the spherical proppant is employed. As analyzed from Figs. 36 and 37, the reason for the production difference in Fig. 38 is proppant embedment, not the fracture conductivity. From previous literature, we note that they attribute the reduction of production to the reduction of fracture conductivity and believe that different proppants lead to different embedding amounts, which leads to different fracture conductivity. The reason is that the discrete fracture model cannot separately consider the fracture conductivity and the permeation ability of the fracture surface.

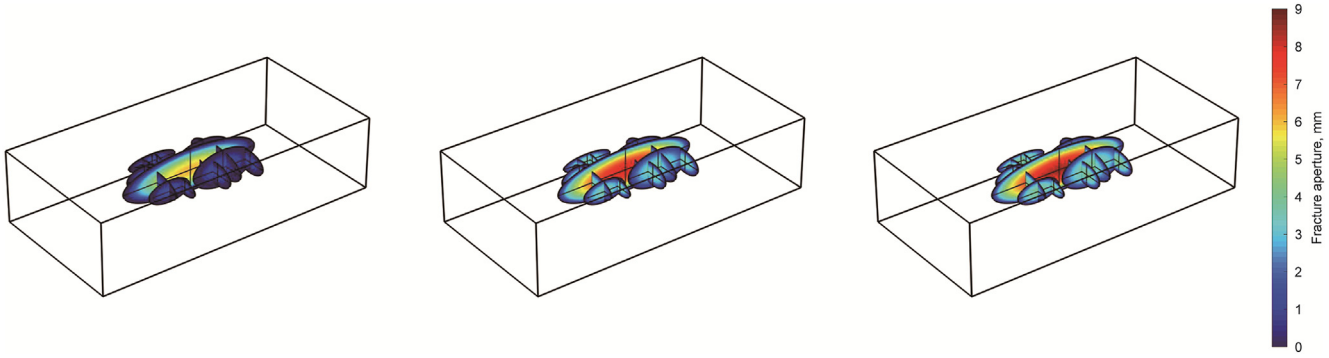

Fig. 29. Effect of fracture surface creep viscosity coefficient on fracture aperture after 1 year of production (from left to right, the creep viscosity coefficient is 1×10^{15}, 1×10^{16}, 1×10^{17} Pa s).

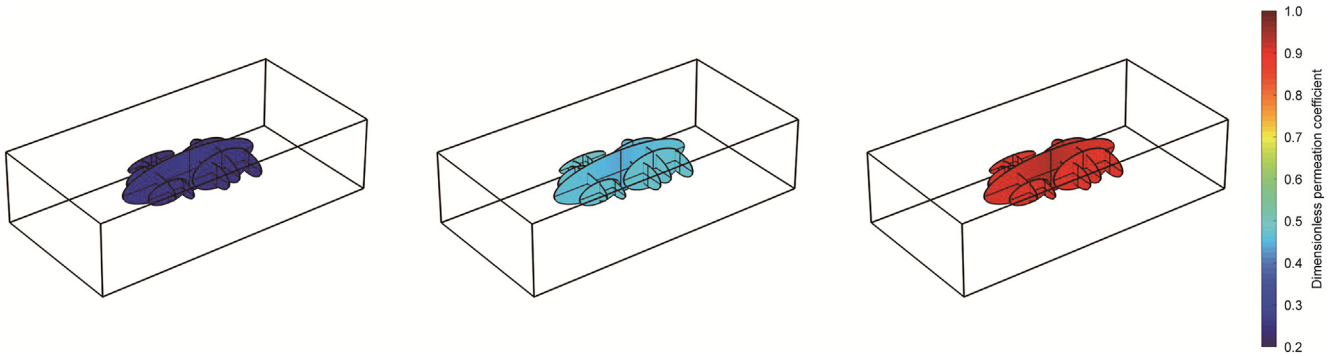

Fig. 30. Effect of fracture surface creep viscosity coefficient on the dimensionless permeation coefficient of fracture surfaces after 1 year of production (from left to right, the creep viscosity coefficient is 1×10^{15}, 1×10^{16}, 1×10^{17} Pa s).

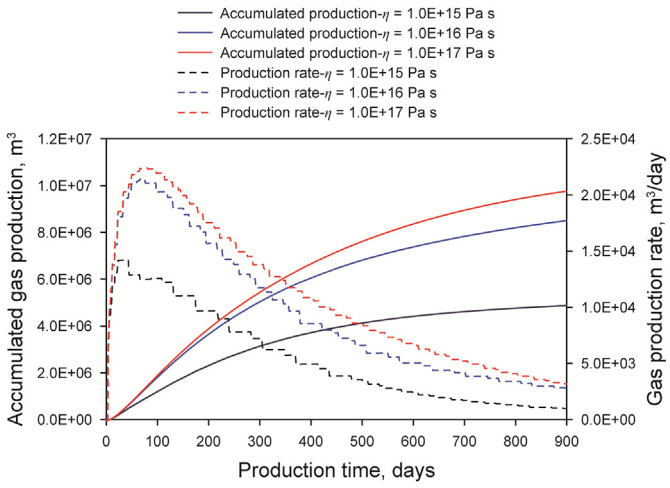

Fig. 31. Effect of fracture surface creep viscosity coefficient on shale gas production.

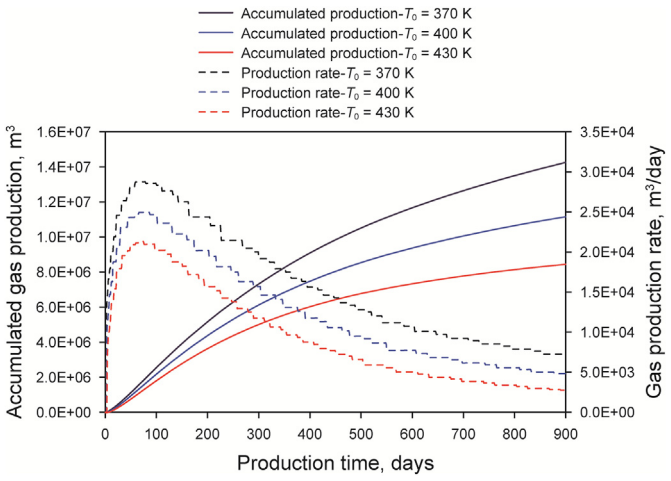

Fig. 33. Effect of initial formation temperature on shale gas production.

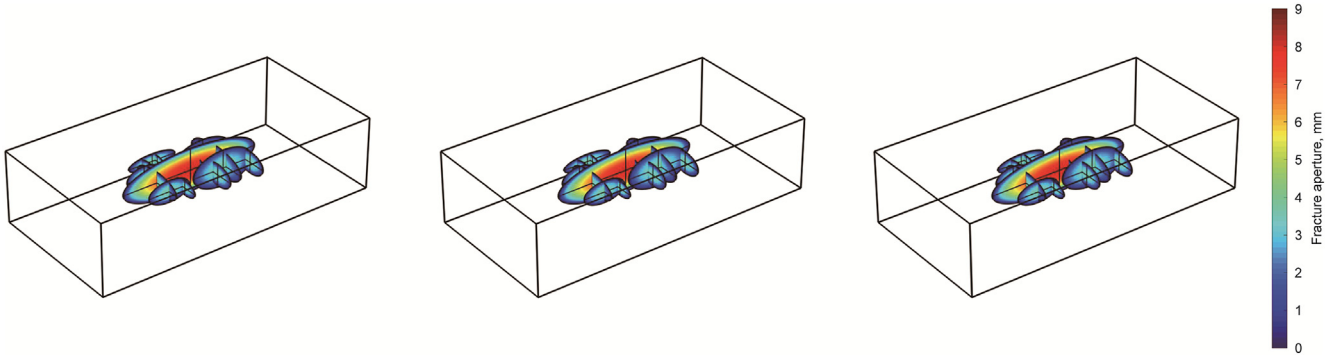

Fig. 32. Effect of initial formation temperature on fracture aperture after 1 year of production (from left to right, the initial formation temperature is 370, 400, 430 K).

5. Conclusions

In this paper, to comprehensively evaluate the effectiveness of the fracture network in the production process, both the fracture closure and the change of the fracture surface permeation coefficient are considered. A fluid–solid–heat coupled model is established, and the discontinuous discrete fracture method is employed to solve the coupled model. The effectiveness of the fracture networks during the production process is mainly evaluated through shale gas production. Furthermore, some conclusions can be drawn from the simulation results.

(1) Shale creep increases the proppant embedment in fracture surfaces, reducing the fracture aperture (i.e., flow conductivity) and the fracture surface permeation coefficient. Under fully equivalent conditions, shale gas production after accounting for shale creep has minimal impact in the first two months, but the accumulated gas production is 42.8% lower after 900 days of production.

(2) When the fracture is well propped, the effect of the proppant embedment on the fracture surface permeation coefficient is more significant than that on the fracture conductivity.

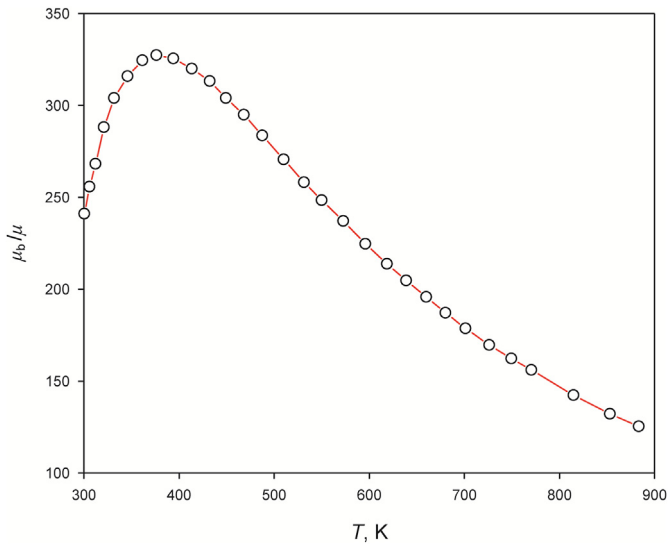

Fig. 34. Relationship between the formation temperature and the ratio of the bulk viscosity to the shear viscosity of CH_4 (Cramer, 2012).

(3) Compared with spherical proppant, cylindrical proppant can reduce the degree of fracture closure and the loss of fracture surface permeation coefficient, thus increasing shale gas production. There is an optimal value for the height-to-diameter ratio of cylindrical proppant. Under the conditions this paper calculated, the optimal height-to-diameter value is 2.
(4) For the deep shale formation, when the formation temperature is higher than 370 K, the gas production decreases with the increase in the formation temperature.

CRediT authorship contribution statement

Shi-Ming Wei: Conceptualization, Funding acquisition, Writing – original draft. **Yang Xia:** Writing – review & editing. **Yan Jin:** Conceptualization, Funding acquisition, Methodology. **Xu-Yang Guo:** Formal analysis, Investigation. **Jing-Yu Zi:** Software, Validation. **Kai-Xuan Qiu:** Data curation, Supervision. **Si-Yuan Chen:** Software, Validation.

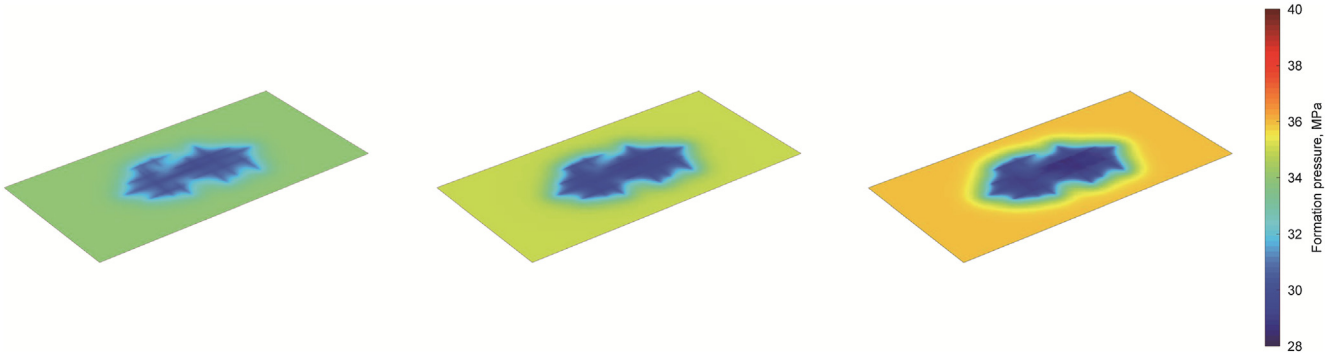

Fig. 35. Effect of initial formation temperature on formation pressure after 900 days of production (from left to right, the initial formation temperature is 370, 400, 430 K).

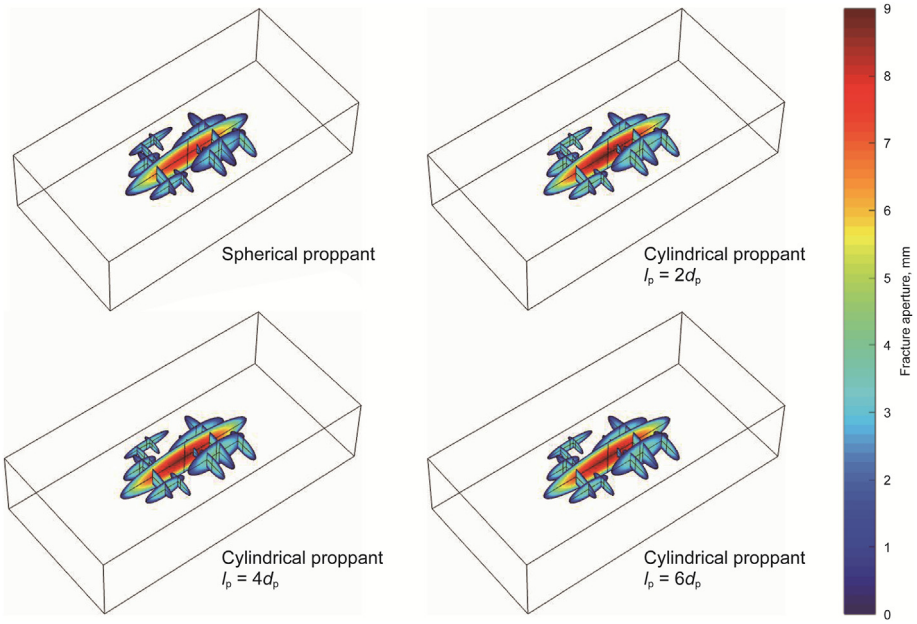

Fig. 36. Fracture aperture with different types of proppants after 1-year production.

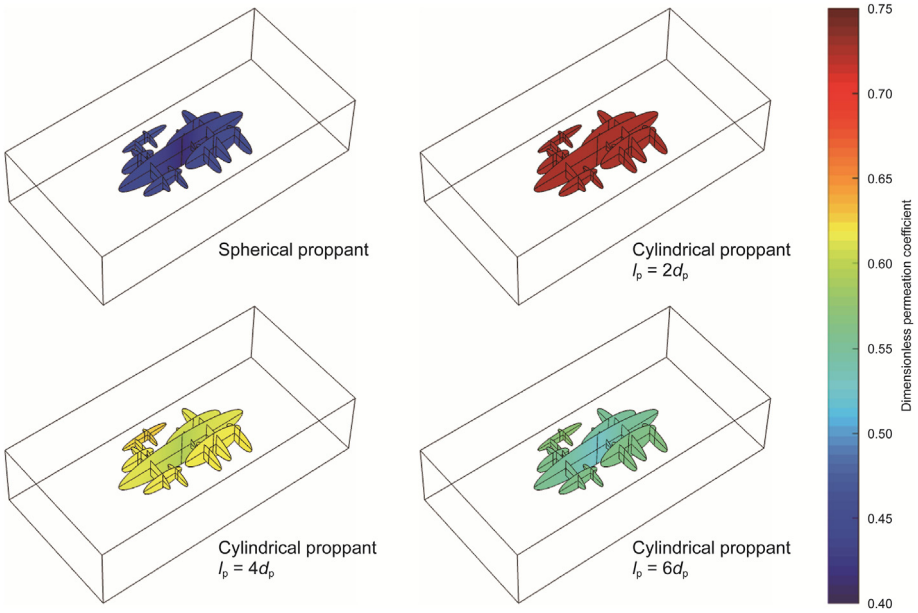

Fig. 37. Dimensionless permeation coefficient of fracture surfaces propped with different types of proppants after 1-year production.

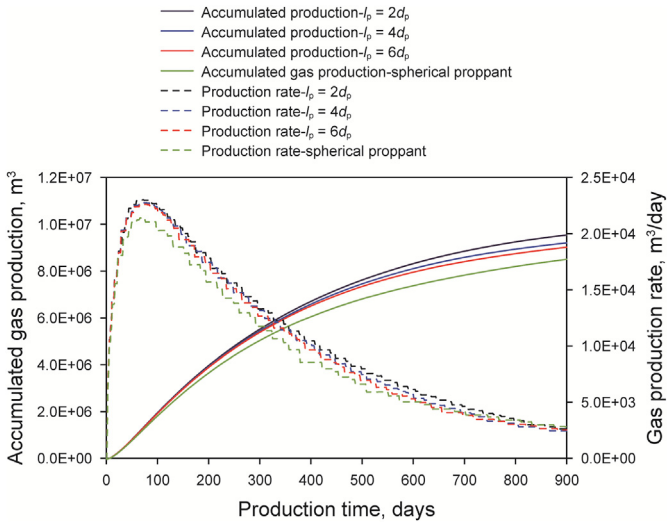

Fig. 38. Shale gas production with different types of proppants.

Declaration of competing interest

The authors declare that they have no known competing financial interests or personal relationships that could have appeared to influence the work reported in this paper.

Acknowledgements

The authors are grateful to the supports provided by China University of Petroleum, Beijing (Grand No. ZX20230042) and the National Natural Science Foundation of China (Grand No. 52334001 and Grand No. 51904314).

References

Akrad, O., Miskimins, J., Prasad, M., 2011. The effects of fracturing fluids on shale rock mechanical properties and proppant embedment. In: SPE Annual Technical Conference and Exhibition. https://doi.org/10.2118/146658-MS.

Chen, H.Y., Teufel, L.W., 1997. Coupling fluid-flow and geomechanics in dual-porosity modeling of naturally fractured reservoirs. In: SPE Annual Technical Conference and Exhibition. https://doi.org/10.2118/38884-MS.

Cramer, M.S., 2012. Numerical estimates for the bulk viscosity of ideal gases. Phys. Fluids 24 (6), 066102. https://doi.org/10.1063/1.4729611.

Cronin, M., Emami-Meybodi, H., Johns, R.T., 2019. Diffusion-dominated proxy model for solvent injection in ultratight oil reservoirs. SPE J. 24 (2), 660–680. https://doi.org/10.2118/190305-PA.

Das, P., Achalpurkar, M., Pal, O., 2014. Impact of formation softening and rock mechanical properties on selection of shale stimulation fluid: laboratory evaluation. In: SPE/EAGE European Unconventional Resources Conference and Exhibition. https://doi.org/10.2118/167787-MS.

Detournay, C., Damjanac, B., Torres, M., et al., 2022. Heat advection and forced convection in a lattice code-Implementation and geothermal applications. Rock Mechanics Bulletin 1 (1), 100004. https://doi.org/10.1016/j.rockmb.2022.100004.

Fan, L., Thompson, J.W., Robinson, J.R., 2010. Understanding gas production mechanism and effectiveness of well stimulation in the haynesville shale through reservoir simulation. In: Canadian Unconventional Resources and International Petroleum Conference. https://doi.org/10.2118/136696-MS.

Freeman, C.M., Moridis, G., Ilk, D., et al., 2013. A numerical study of performance for tight gas and shale gas reservoir systems. J. Petrol. Sci. Eng. 108, 22–39. https://doi.org/10.1016/j.petrol.2013.05.007.

Gao, J., Deng, J., Lan, K., et al., 2017. A porothermoelastic solution for the inclined borehole in a transversely isotropic medium subjected to thermal osmosis and thermal filtration effects. Geothermics 67, 114–134. https://doi.org/10.1016/j.geothermics.2017.01.003.

Heidaryan, E., Moghadasi, J., Rahimi, M., 2010. New correlations to predict natural gas viscosity and compressibility factor. J. Pet. Sci. Eng. 73 (1–2), 67–72. https://doi.org/10.1016/j.petrol.2010.05.008.

Jin, Y., Chen, K.P., 2019. Fundamental equations for primary fluid recovery from porous media. J. Fluid Mech. 860, 300–317. https://doi.org/10.1017/jfm.2018.874.

Jin, Y., Wei, S., Chen, K., et al., 2020. Self-diffusion flow model of tight gas. Acta Pet. Sin. 41 (6), 737–744. https://doi.org/10.7623/syxb202006008 (in Chinese).

Johnson, K.L., 1987. Contact Mechanics. Cambridge University Press.

Klainerman, S., Majda, A., 1982. Compressible and incompressible fluids. Commun. Pure Appl. Math. 35, 629–651.

Lacy, L.L., Rickards, A.R., Bllden, D.M., 1998. Fracture width and embedment testing in soft reservoir sandstone. SPE Drill. Complet. 13 (1), 25–29. https://doi.org/10.2118/36421-PA.

Liu, Y., Leung, J.Y., Chalaturnyk, R.J., et al., 2019. New insights on mechanisms controlling fracturing-fluid distribution and their effects on well performance in shale-gas reservoirs. SPE Prod. Oper. 34 (3), 564–585. https://doi.org/10.2118/185043-PA.

Lu, Y., Wei, S., Xia, Y., et al., 2021. Modeling of geomechanics and fluid flow in fractured shale reservoirs with deformable multi-continuum matrix. J. Petrol. Sci. Eng. 196, 107576. https://doi.org/10.1016/j.petrol.2020.107576.

Puttock, M.J., Thwaite, E.G., 1969. Elastic Compression of Spheres and Cylinders at Point and Line Contact. Commonwealth Scientific and Industrial Research Organization, Melbourne, Australia.

Valliappan, S., Khalili-Naghadeh, N., 1990. Flow through fissured porous media with deformable matrix. Int. J. Numer. Methods Eng. 29 (5), 1079–1094. https://doi.org/10.1002/nme.1620290512.

Wang, P., 2015. Mechanics Research on Creep Buckling of the Shale Hydration Damage. Ph.D. Dissertation. Northwestern Polytechnical University.

Wei, S., Xia, Y., Jin, Y., et al., 2019. Quantitative study in shale gas behaviors using a coupled triple-continuum and discrete fracture model. J. Petrol. Sci. Eng. 174, 49–69. https://doi.org/10.1016/j.petrol.2018.10.084.

Wei, S., Kao, J., Jin, Y., et al., 2021. A discontinuous discrete fracture model for coupled flow and geomechanics based on FEM. J. Petrol. Sci. Eng. 204, 108677. https://doi.org/10.1016/j.petrol.2021.108677.

Wei, S., Jin, Y., Wang, S., et al., 2022. A framework to obtain the formulas of the conductivity and aperture of rough fractures under thermohydromechanical conditions. J. Petrol. Sci. Eng. 208, 109354. https://doi.org/10.1016/j.petrol.2021.109354.

Xia, Y., Wei, S., Jin, Y., et al., 2021. Self-diffusion flow and heat coupling model applicable to the production simulation and prediction of deep shale gas wells. Nat. Gas. Ind. 41 (2), 111–118 (in Chinese).

Yan, X., Huang, Z., Zhang, Q., et al., 2020. Numerical investigation of the effect of partially propped fracture closure on gas production in fractured shale reservoirs. Energies 13 (20), 5339. https://doi.org/10.3390/en13205339.

Zhou, L., Shen, Z., Wang, J., et al., 2019. Numerical investigating the effect of nonuniform proppant distribution and unpropped fractures on well performance in a tight reservoir. J. Petrol. Sci. Eng. 177, 634–649. https://doi.org/10.1016/j.petrol.2019.02.086.